

1 Kinematics and Detector Designs for the different EIC Machine Designs

E.C. Aschenauer, R. Ent, T. Horn, P. Nadel-Turonski, H. Spiesberger

1.1 Kinematics and Requirements for an EIC Detector

The physics program of an EIC imposes several challenges on the design of a detector, and more globally the extended interaction region, as it spans a wide range in center-of-mass energy, different combinations of both beam energy and particle species, and several different physics processes. The various physics processes encompass inclusive measurements ($ep/A \rightarrow e' + X$), which require detection of the scattered lepton and/or the full scattered hadronic debris with high precision; semi-inclusive processes ($ep/A \rightarrow e' + h + X$), which require detection in coincidence with the scattered lepton of at least one (current or target region) hadron; and exclusive processes ($ep/A \rightarrow e' + N'/A' + \gamma/m$), which require detection of all particles in the reaction. The following figures in this Section demonstrate the differences in particle kinematics of some representative examples of these reaction types, as well as differing beam energy combinations. For these plots the directions of the beams are defined as for HERA at DESY: the hadron beam is in the positive z direction (0°) and the lepton beam is in the negative z -direction (180°). The upper panel of Fig. 1 illustrates that the lower Q^2 is, the closer the momentum of the scattered lepton is to the original lepton beam energy. For all lepton-hadron beam energy combinations (indicated by the panel in each of the plots), the scattered lepton goes in the direction of the original lepton beam for low Q^2 and more and more into a central detector acceptance for higher Q^2 . For a fixed hadron beam energy the lepton scattering angle becomes smaller at a fixed Q^2 with increasing lepton energy.

Figure 2 shows the x - Q^2 plane for two different center-of-mass energies. In general, the correlation between x and Q^2 for a collider environment is weaker than for fixed target experiments. Nonetheless, it becomes stronger for small scattering angles or corresponding small inelasticity y , and momentum and scattering angle resolution for the scattered lepton become an issue, at HERA roughly at $y = 0.1$. To circumvent this problem, HERA reconstructed the lepton kinematics from the hadronic final state using the Jacquet-Blondel method [1, 2], and has reached successful measurements down to y of 0.005. The main reason why this hadronic method renders better resolution at low y follows from the equation $y_{JB} = E - P_z^{had}/2E_e$, where $E - P_z^{had}$ is the sum over the energy minus the longitudinal momentum of all hadronic final-state particles and E_e is the electron beam energy. This quantity has no degradation of resolution for $y < 0.1$ as compared to the electron method, where $y_e = 1 - (1 - \cos\theta_e)E'_e/2E_e$. This is directly correlated to the relative resolutions for both quantities: $\Delta y_{JB}/y_{JB} \sim \text{constant}$ and $\Delta y_e/y_e \sim 1/y_e$.

Typically, one can obtain for a given center-of-mass energy squared roughly a decade of Q^2 reach at fixed x when using only an electron method to determine lepton kinematics, and roughly two decades when including the hadronic method. If only using the electron method, one can increase the range in accessible Q^2 by lowering the center-of-mass energy, as can be seen from comparing the two panels of Figure 2. This may become relevant for some semi-inclusive and exclusive processes. The advantages and disadvantages of this solution are discussed in the two machine-specific detector sections of this Section.

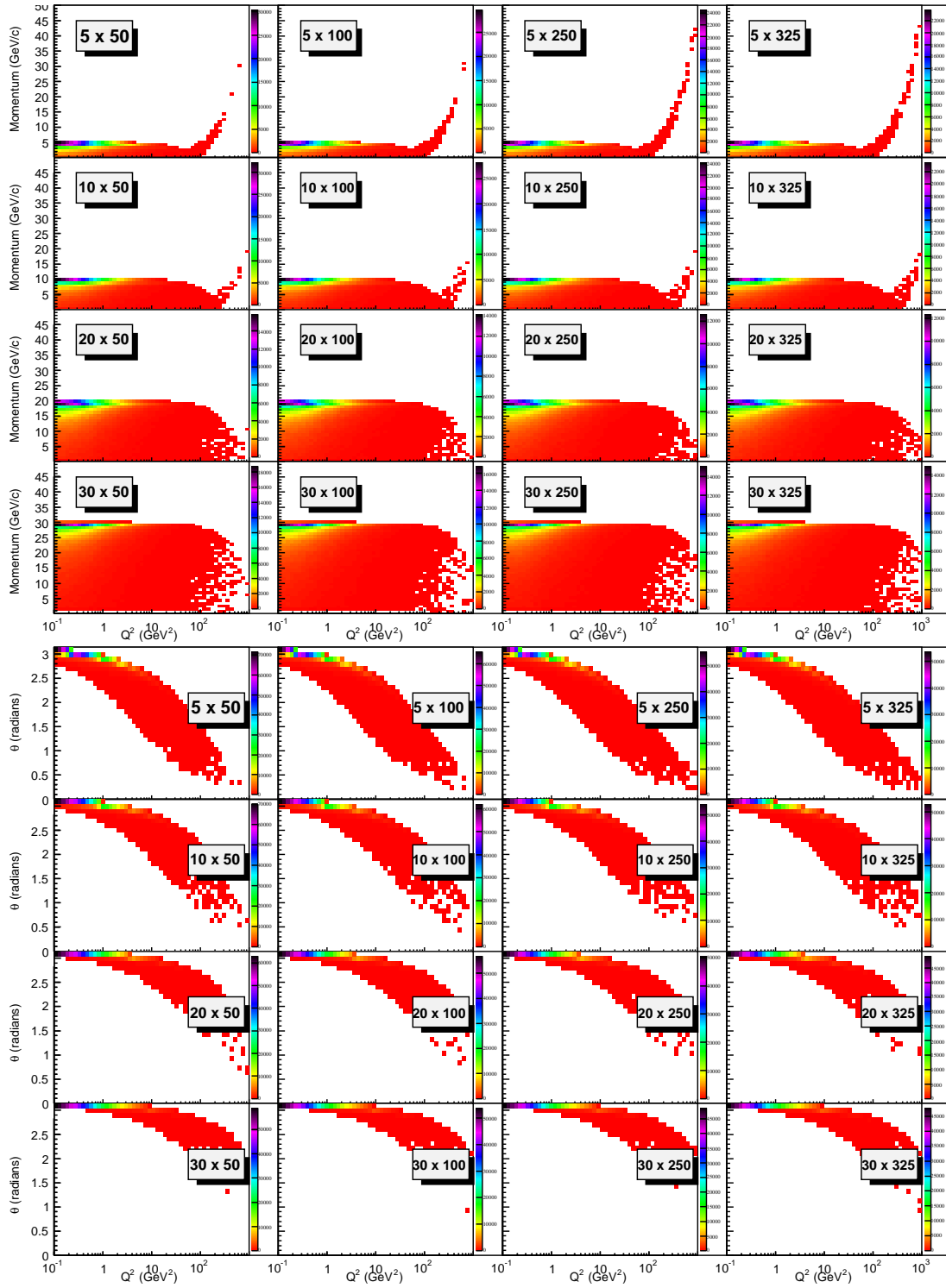


Figure 1: Q^2 vs. momentum (upper panel) and Q^2 vs. scattering angle (lower panel) of the scattered lepton in the laboratory frame. The following cuts have been applied in both figures: $Q^2 > 0.1$ GeV², $0.01 < y < 0.95$. The lepton-hadron beam energy combinations are indicated by the panel in each individual plots

In general, one would like to access as large a range in Q^2 at fixed x as possible for a given beam energy combination, and reach as low y_{JB} as possible. This requirement directly implies two important considerations for the detector design:

- good hadronic coverage in forward direction
- low noise and/or good noise suppression algorithms in the hadronic calorimeter to allow for hadron detection down to 0.5 GeV. More detailed detector simulations have to firm this requirements.

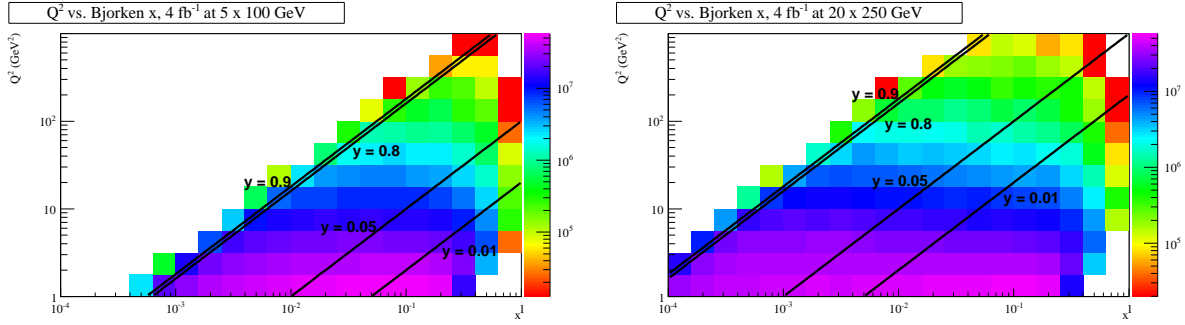


Figure 2: The x - Q^2 plane for center-of-mass energy 45 GeV (left) and 140 GeV (right). The black lines indicate different y -cuts placed on the scattered lepton kinematics.

It is important to point out that the reconstruction of the event kinematics from the hadronic final state is also important in suppressing events with radiation of a real or virtual photon from the incoming or outgoing lepton (radiative corrections); for details please see section 1.2.

One should keep in mind that there are additional complications at low y for the measurement of asymmetries and/or polarized cross sections, to for example extract the helicity-dependent parton distributions. A depolarization factor, defined as $D = \frac{y[(1+\gamma^2 y/2)(2-y)-2y^2 m_e^2/Q^2]}{y^2(1-2m_e^2/Q^2)(1+\gamma^2)+2(1+R)(1-y-\gamma^2 y^2/4)}$ [3] is needed to correct the measured helicity-dependent asymmetries ($A_{||}$). The depolarization factor corrects for the polarization transfer from the lepton to the virtual photon, and is small at low y . This reduces the effective polarized luminosity and increases the uncertainties of the measured polarized quantities at low y ($\delta A_1 = \delta A_{||}/D$). Therefore, the x - Q^2 -plane of precision polarized cross section measurements will be reduced as compared to unpolarized ones, for fixed center-of-mass energy.

Figure 3 shows the momentum versus scattering angle distributions in the laboratory frame for pions originating from semi-inclusive reactions, for different lepton and proton beam energy combinations. For lower lepton energies pions are scattered more in the forward (ion) direction. For fixed low lepton energy of 5 GeV, this pattern remains more or less constant as function of proton energy. With increasing lepton beam energy, the hadrons increasingly populate the central region of the detector, and at the highest lepton energies hadrons are even largely produced going backward (i.e. in the lepton beam direction). The kinematic distributions for kaons and protons, applying the same cuts as for pions, are essentially identical to those of the pions. The distributions for semi-inclusive events in electron nucleus collisions may be slightly altered due to nuclear modification effects, but the global features will remain.

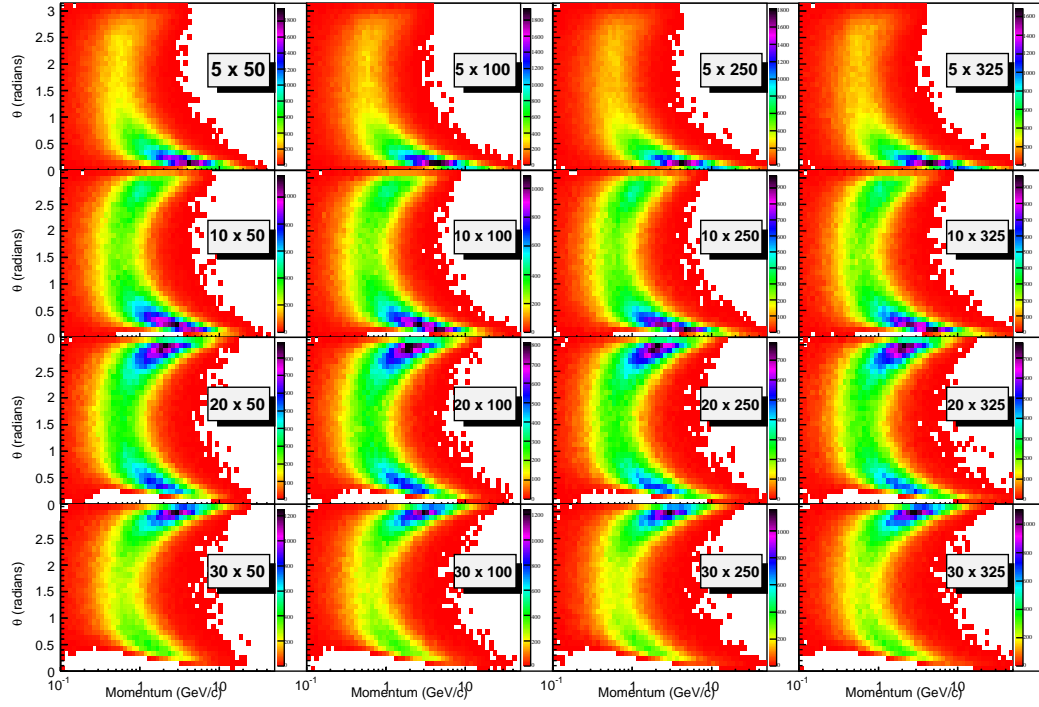


Figure 3: Momentum vs. scattering angle in the laboratory frames for pions from non-exclusive reactions. The following cuts have been applied: $Q^2 > 1 \text{ GeV}^2$, $0.01 < y < 0.95$ and $0.1 < z < 0.9$

Fig. 3 also indicates a shift of the momentum range of pions towards higher momenta in the central-angle region for higher lepton energy, to typical momenta of about 10 GeV/c, which has implications for the required particle identification (PID). To be able to identify the different hadron types over a wide momentum and angular range an EIC detector needs to have detectors capable of good PID in the forward, central and backward direction. For the higher hadron momenta, typically in the forward ion direction and also in the backward direction for higher lepton beam energies, the most viable detector technology is a Ring-Imaging Cherenkov (RICH) detector with dual-radiators. In the central detector region a combination of high resolution time-of-flight (ToF) detectors (preferentially with timing resolutions $\delta t \sim 10\text{ps}$), a DIRC or a proximity focusing Aerogel RICH may be adequate detector technologies.

For certain kinematics the hadrons (both charged and neutral) will be produced in the backward ion direction (see Fig. 4), and need to be disentangled from the scattered leptons. The kinematic region in rapidity η over which hadrons and photons need to be suppressed with respect to electrons shifts to more negative rapidity with increasing center-of-mass energy. This can be cross-correlated with the angular and momentum patterns for scattered leptons of Fig. 1. For the lower center-of-mass combination, electron, photon and charged hadron rates are roughly comparable at 1 GeV/c total momentum and $\eta = -3$. For the higher center-of-mass energy, electron rates are a factor of 10-100 smaller than photon and charged hadron rates, and comparable again at a 10 GeV/c total momentum.

This adds another requirement to the detector: good electron identification. The kinematic region in rapidity η over which hadrons and also photons need to be suppressed, typically by a factor of 10 - 100, shifts to more negative rapidity with increasing center-

of-mass energy. Measuring the ratio of the lepton energy and momentum, E'_e/p'_e , typically gives a reduction factor of ~ 100 for hadrons. This requires the availability of both tracking detectors (to determine momentum) and electromagnetic calorimetry (to determine energy) over the same rapidity coverage. This availability also immediately suppresses the misidentification of photons in the lepton sample, by requiring that a track must point to the electromagnetic cluster. Of course, the availability of good tracking detectors over similar coverage as electromagnetic calorimetry similarly aids in y resolution at low y from a lepton method only (see earlier), as the angular as well as the momentum resolution for trackers are much better than for electromagnetic calorimeters. The hadron suppression can be further improved by adding a Cherenkov detector to the electromagnetic calorimetry. Combining the electromagnetic calorimeter response and the response of Cherenkov detectors may especially help in the region of low-momentum scattered leptons, about 1 GeV/c. Other detector technologies, such as transition radiation detectors, may provide another factor 100 hadron suppression for lepton momenta greater than 4 GeV/c.

An additional advantage of a collider detector over a fixed target experiment is the large coverage in transverse momentum. This is especially important for measurements linking the perturbative high-transverse momentum p_T region to the region of small transverse momentum, $p_T \sim \Lambda$, where single-spin asymmetries as function of p_T, x, Q^2, z and ϕ are the prime observable to extract TMDs - Transverse Momentum Dependent Parton Distributions (see section ??), like the Sivers function. Fig. 5 shows the coverage in hadron p_T measured with respect to the virtual photon vs. $z = E_h/\nu$ assuming an angular acceptance of a detector $0.5^\circ < \theta < 179.5^\circ$. One can see that for all beam energy combinations a large range in transverse momentum is achievable. In general, such physics does not drive the most forward (or backward) detector requirements, leaving ample of phase space in transverse momentum with respect to the virtual-photon direction - typically more central.

There is specific interest in detecting events with heavy quarks (charm or bottom). To measure the inclusive structure functions, F_2^c , F_L^c , and F_2^B for heavy quarks, it is sufficient to tag the charm and the bottom quark content via detection of additional leptons (electron, positron, muons) to the scattered lepton. The leptons from charmed mesons can be identified via a displaced vertex of the second lepton ($\langle \tau \rangle \sim 150 \mu\text{m}$). This can be achieved by integrating a high-resolution vertex detector into the detector design. For measurements of the charmed (bottom) fragmentation functions, or to study medium modifications of heavy quarks in the nuclear environment, at least one of the charmed (bottom) mesons must be completely reconstructed to have access to the kinematics of the parton. This requires, in addition to measuring the displaced vertex, good particle identification to reconstruct the meson via its hadronic decay products, e.g. $D_0 \rightarrow K^\pm + \pi^\mp$.

Figure 6 (upper panel) shows the momentum versus scattering angle distributions for pions following from an exclusive reaction with a ρ^0 vector meson production ($Q^2 > 1.0 \text{ GeV}^2$), in the laboratory frame and for different beam energy combinations. As in Fig. 3, two familiar patterns arise. For increasing lepton beam energy the pion distribution goes from being more peaked in the forward-angle direction to a distribution with both a peak in the forward and backward ion direction, and the momentum in the forward-ion direction is slightly reduced. Most of the forward-ion direction pions in Fig. 6 are correlated with lower- Q^2 processes though, possibly of less interest for these processes. If one would imply a $Q^2 > 10 \text{ GeV}^2$ cutoff in these exclusive processes, only a peak in the backward-ion direction would remain, and in that sense lower lepton energies correspond to lower hadron momenta on average and reduced Particle identification requirements. The distributions for kaons from exclusive ϕ -mesons production as well as for muons/electrons from exclusive

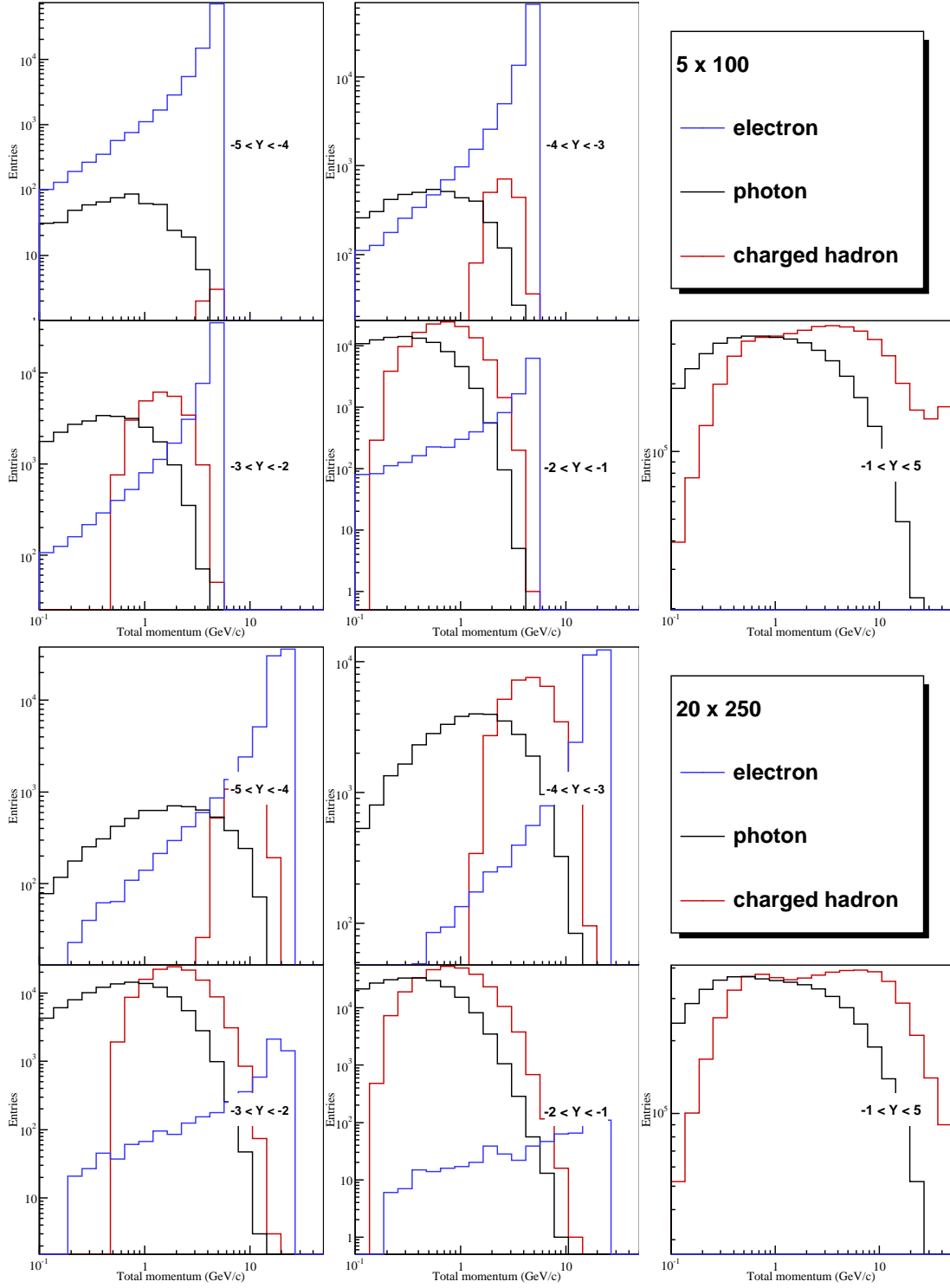


Figure 4: The number of photons and hadrons as well as the number of scattered leptons in a rapidity bin vs momentum having 5 GeV leptons colliding with 100 GeV protons and 20 GeV leptons colliding with 250 GeV protons. No kinematic cuts are applied.

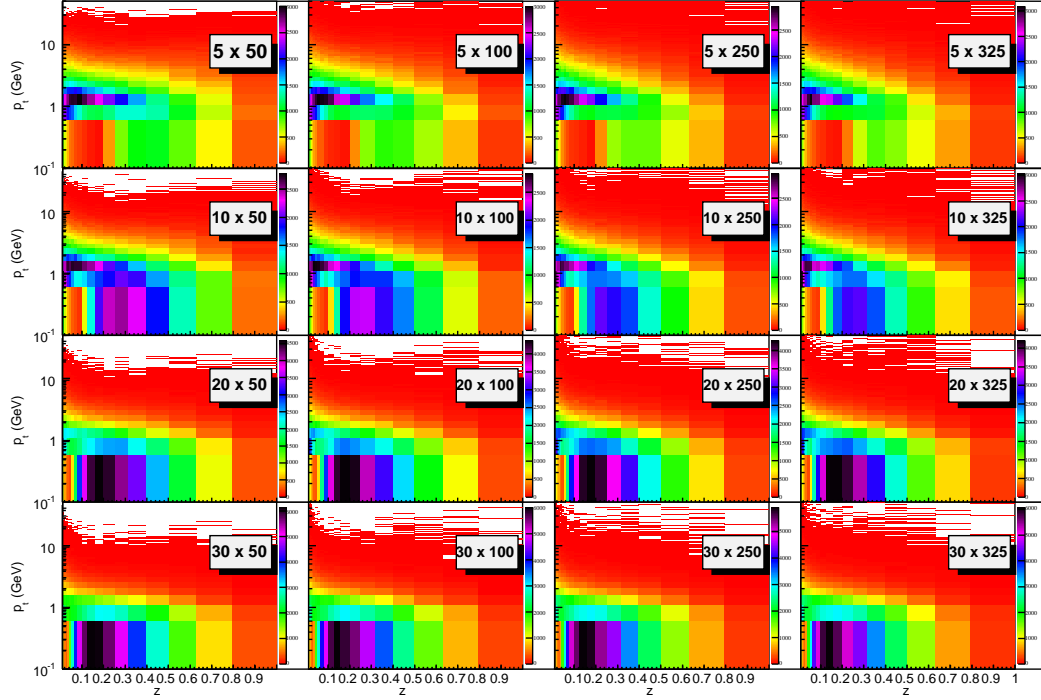


Figure 5: Transverse momentum vs. z for pions applying the following cuts $Q^2 > 1 \text{ GeV}^2$, $0.01 < y < 0.95$, $0.5^\circ < \theta < 179.5^\circ$ and $p > 1 \text{ GeV}$. A momentum cut is applied to simulate the threshold of potential particle-identification-detectors.

J/ψ production look very similar, see lower panel 6. The most challenging constraints on the detector design for exclusive reactions compared to semi-inclusive reactions is, however, not given by the hadrons originating from vector mesons, but from the detection of the exclusive hadronic state remaining.

As one specific example of an exclusive reaction, deeply virtual compton scattering (DVCS) was chosen, Fig. 7 (top) shows the energy versus scattering angle distributions of photons in the laboratory frame, for different beam energy combinations. A cut of $Q^2 > 1 \text{ GeV}^2$ is assumed, although larger values of Q^2 may be required. Lower lepton energies show a more symmetric distribution, and higher lepton energies are more backward-ion angle peaked. The distributions show relatively homogeneous distributions of the DVCS photons from forward to backward, with a small preference for the backward direction. The latter is true for all lepton-hadron beam energy combination.

Figure 7 (bottom) correlates the distribution of the photon angle and the electron scattering angle in the laboratory frame, for different beam-energy combinations. With increasing lepton beam energy the photon and scattered lepton tend towards the same detector hemisphere. Following fig. 7 (top), electromagnetic calorimetry is required over the entire rapidity range of the detector. Figure 7 (bottom) illustrates that tracking and electromagnetic calorimetry capabilities covering similar rapidity range will greatly aid the separation of the photon and lepton, reducing a difficulty encountered by the ZEUS collaboration in their DVCS event reconstruction.

For exclusive reactions in general, with DVCS as the example above, it is extremely important to ensure the remaining nucleon (or the nucleus) remains intact during the scat-

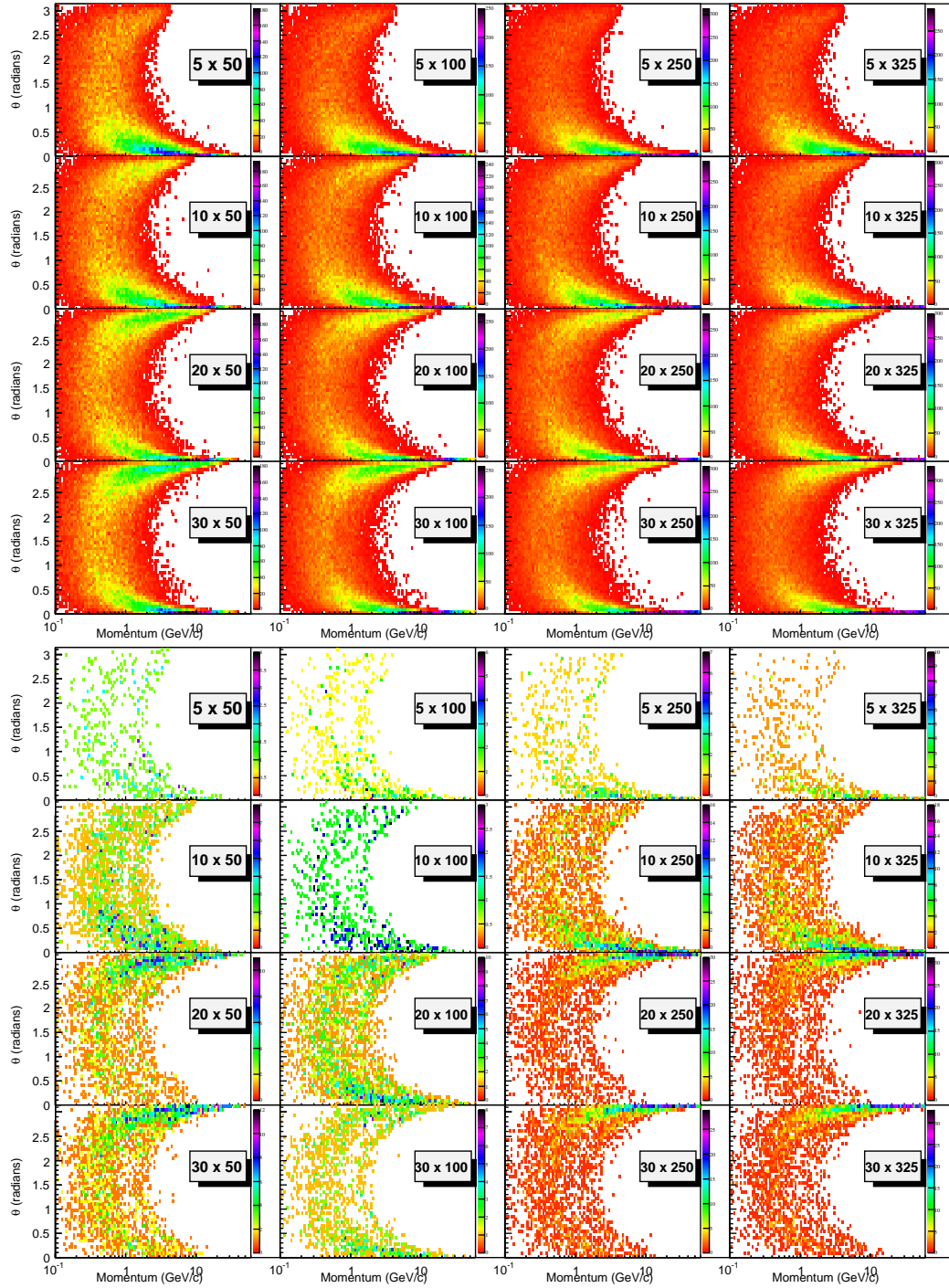


Figure 6: Upper Panel: Momentum vs. scattering angle in the laboratory frames for pions following from exclusive ρ^0 vector meson production. The following cuts are applied: $Q^2 > 1.0 \text{ GeV}^2$, $0.01 < y < 0.95$.

Lower Panel: Momentum vs. scattering angle in the laboratory frames for muons following from exclusive J/ψ vector meson production. No cuts on Q^2 have been applied as a hard scale for the process is given by the J/ψ mass.

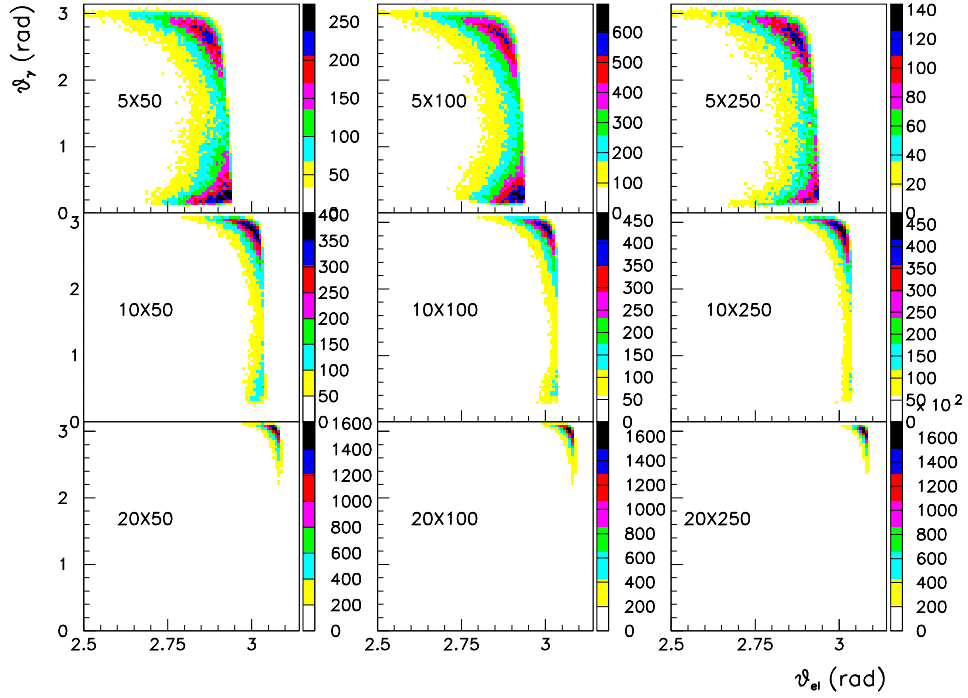
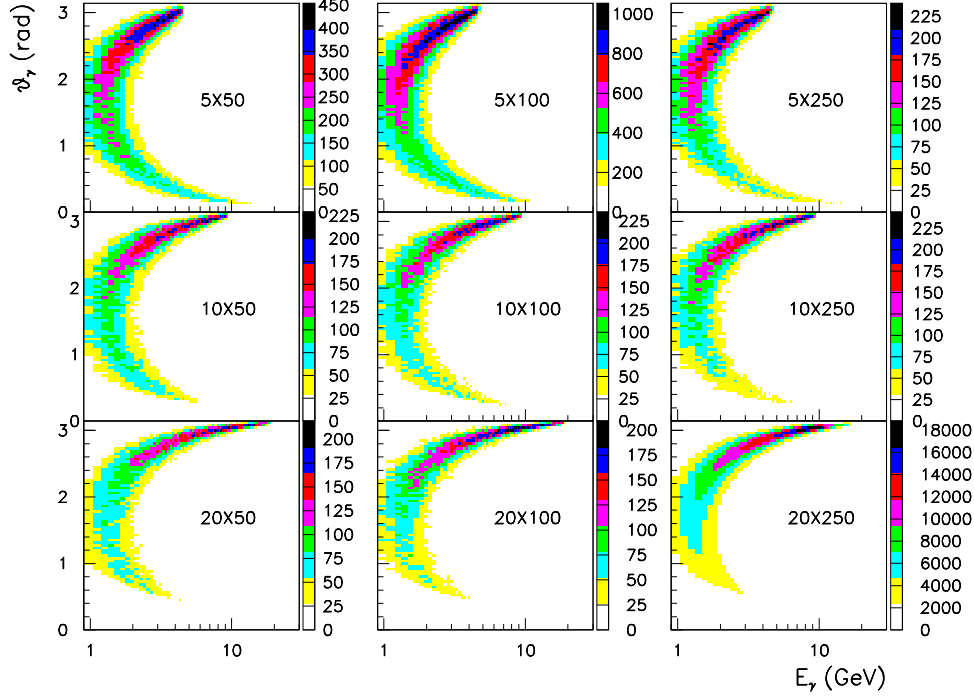


Figure 7: Upper panel: Energy vs. scattering angle in the laboratory frame for photons from DVCS. The following cuts have been applied: $Q^2 > 1.0 \text{ GeV}^2$, $0.01 < y < 0.95$ and $E_\gamma > 1. \text{ GeV}$. Lower Panel: The scattering angle in the laboratory frame of the photon vs. that of the scattered lepton for DVCS events. The following cuts have been applied: $Q^2 > 1.0 \text{ GeV}^2$, $0.01 < y < 0.95$ and $E_\gamma > 1. \text{ GeV}$

tering process. Hence, one has to ensure exclusivity by measuring all products. Figure 8 illustrates the kinematic requirements for the DVCS case, showing the scattered proton momentum versus its scattering angle for three different beam energy combinations. In general, for exclusive reactions one wishes to map the four-momentum transfer (or Mandelstam variable) t to the hadronic system, and then obtain an image by a Fourier transform, at relatively low t of up to 1-2 GeV. The angle of the recoiling hadronic system is directly correlated with t and the proton energy E_p , as \sqrt{t}/E_p . As can be seen in Fig. 8, the proton scattering angle requirements indeed linearly (and inversely) scale with proton energy.

Even at a proton energy of 50 GeV, the proton scattering angles only range to about 1-2°. At proton energies of 250 GeV, this number is reduced to one/fifth. In all cases, one obtains small to extremely small scattering angles, extending to or completely within the 0.5° angular detector cutoff often used above. Because of this, the detection of these protons, or more general recoil baryons, is extremely dependent on the exact interaction region design and will therefore be discussed in more detail in the machine-dependent part of this chapter.

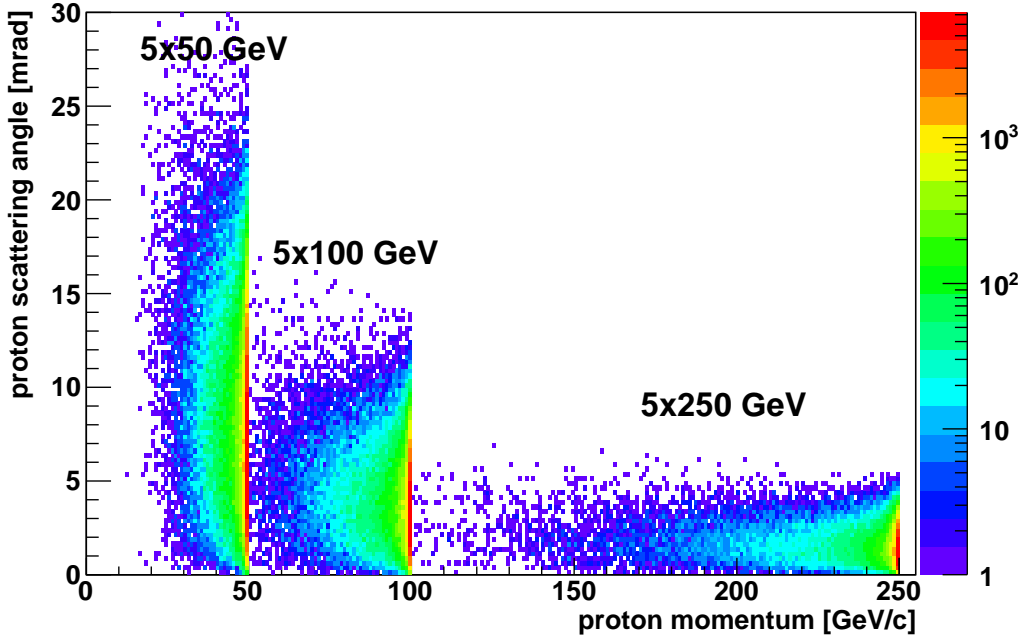


Figure 8: Scattered proton momentum vs. scattering angle in the laboratory frames for DVCS events with different beam energy combinations. The following cuts have been applied: $1 \text{ GeV}^2 < Q^2 < 100 \text{ GeV}^2$, $10^{-5} < x < 0.7$ and $0 < t < 2 \text{ GeV}^2$.

Detection of the intact nucleus following an exclusive reaction in eA collisions is even more complicated. The binding energy in heavy nuclei is of the order 8 MeV per nucleon. In general, the smallest measurable outgoing angle of heavy scattered or fragmented nuclei, θ_{min} , is limited by the beam angular divergence and the requirement to have a $\sim 10 \sigma$ clearance of any detector element (often 'Roman pots') from the beam. For a beam divergence of say 0.1 mrad and an ion beam of 100 GeV/u, the transverse momentum required in the nuclear breakup to be beyond the so-called machine 'beam-stay-clear' area of $\sim 10 \sigma$ is 100

MeV, well beyond the 8 MeV (or so) needed for a single nucleon. This would assume that the transverse momentum is equal to the coherent to the excitation energy of the nucleus.

The diffractive slope at $t = 0$ depends on the size of the nucleus. Figure ?? shows, for small $t \sim 1/R_A^2$, a very steep t dependence, $\sim \exp(-tR_A^2/3)$, and then several diffractive minima ($R_A = (1.12\text{fm})A^{1/3} - (0.86\text{fm})A^{-1/3}$, for details see [4]). The incoherent background starts to dominate at t values at which the coherent cross section has fallen to $1/e$. This t values can be estimated by $\exp(-|t|B_0A^{2/3}) = 1/A$, with $B_0 = (1.12\text{fm})^{2/3}$. These values of t are much smaller than the t value corresponding to the first minimum in the coherent cross section and the t -values corresponding to the smallest measurable outgoing angle of scattered heavy nuclei. Therefore the strategy to ensure exclusive production on a nucleus is to veto nuclear breakup, by detecting the neutrons from incoherent events.

Another possibility can be to require a rapidity gap between the hadron beam and the produced jet, (vector) meson or real photon (where all events represent the sum of elastic and incoherent events). The left panel of figure 9 shows the rapidity distribution of the most forward particle in deep-inelastic scattering (blue filled distribution) and diffractive events (unfilled histogram), respectively, for a 5 GeV electron and a 100 GeV proton beam energy combination. The 100 GeV is here chosen to mimic the 100 GeV/u ion beam. The right panel of figure 9 shows the efficiency and purity for diffractive events to DIS events (1:1) as function of rapidity, varying the lepton beam energy while keeping the hadron beam energy fixed. If one requires 4 units of rapidity between the hadron beam and a produced jet, vector meson or real photon, an efficiency of above 60% and a purity close to 100% for diffractive events would be obtained. A detector with wide rapidity coverage is essential for

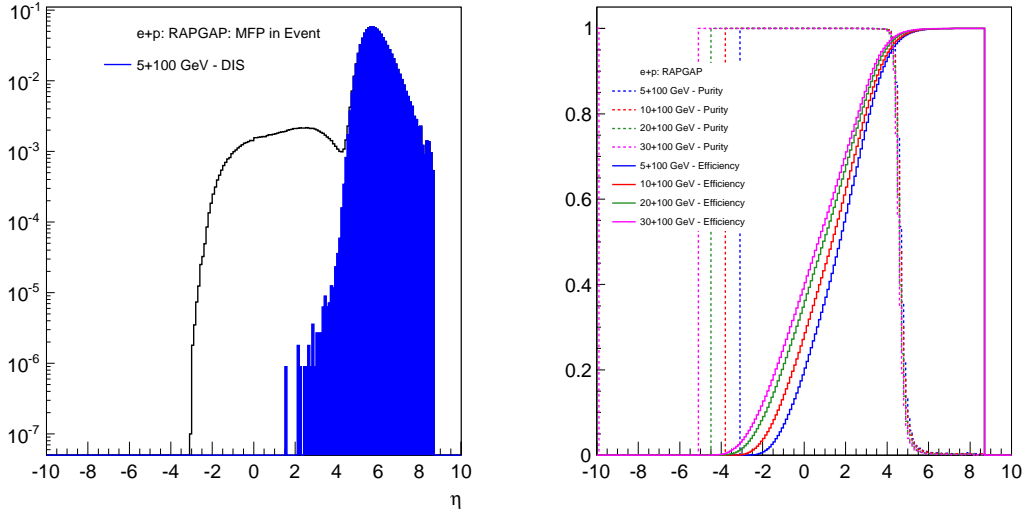


Figure 9: Left: Rapidity distribution of DIS and diffractive events for the most forward particle (MFP) in the event. Right: Efficiency and Purity for diffractive events with respect to DIS events (1:1) as a function of the detector rapidity coverage and the center-of-mass energy.

such events.

1.2 Radiative Corrections

The radiation of real and virtual photons leads to large additional contributions to the observable cross section of electron scattering at high energies. Precision measurements of the nucleon structure require a good understanding of these radiative corrections. For neutral-current lepton nucleon scattering, a gauge-invariant classification into leptonic, hadronic and interference contributions can be obtained from Feynman diagrams. The Feynman diagrams for leptonic corrections are shown in figure 10. Leptonic corrections dominate and strongly affect the experimental determination of kinematic variables.

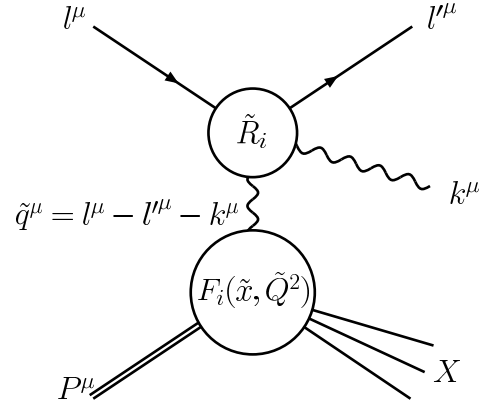
Usually, the cross section is measured as a function of Q^2 and Bjorken- x , x_B , defined as

$$Q^2 = -(l - l')^2, \quad x_B = \frac{Q^2}{2P \cdot (l - l')}, \quad (1)$$

where l and l' denote the 4-momenta of the incoming and outgoing lepton, respectively, and P is the 4-momentum of the incoming nucleon. The true values of these variables seen by the nucleon when a photon with 4-momentum k is radiated are, however, given by (see figure)

$$\tilde{Q}^2 = -(l - l' - k)^2, \quad \tilde{x}_B = \frac{\tilde{Q}^2}{2P \cdot (l - l' - k)}. \quad (2)$$

If the photon momentum is large and balancing the transverse momentum of the scattered lepton, \tilde{Q}^2 can be shifted to small values, leading to an enhancement of the radiative corrections. This effect is similar to the radiative tail of a resonance.



Kinematics of leptonic radiation.

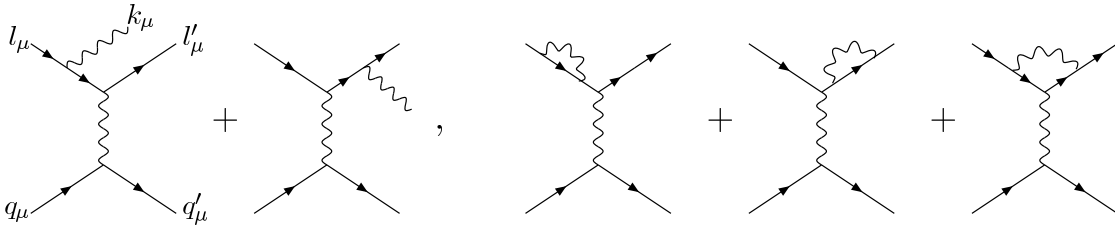


Figure 10: Feynman diagrams for leptonic radiation in lepton-quark scattering.

The effect of radiation of photons from the lepton can be described with the help of radiator functions $\tilde{R}_i(l, l', k)$. There is one \tilde{R}_i for every structure function F_i , $i = 2, L$. The radiator functions comprise both real radiation from the initial and the final state as well as the contribution from vertex and self-energy diagrams. Using \tilde{x}_B and \tilde{Q}^2 from equation (2) to parametrize the integration over the phase space of emitted photons, one can express the observed structure functions as convolutions,

$$F_i^{\text{obs}}(x_B, Q^2) = \int d\tilde{x}_B d\tilde{Q}^2 R_i(x_B, Q^2, \tilde{x}_B, \tilde{Q}^2) F_i^{\text{true}}(\tilde{x}_B, \tilde{Q}^2). \quad (3)$$

The integration limits are determined by the energy allowed for the radiated photon which, in the photon-nucleon center-of-mass frame, is given by

$$E_{\gamma}^{\max} = \sqrt{\frac{1-x_B}{x_B}} Q^2. \quad (4)$$

Radiative corrections are, therefore, large at large Q^2 and small x_B . In contrast, at small Q^2 and large x_B , the phase space for photon emission is restricted and negative virtual corrections dominate.

From equation (3) it is obvious that the determination of the true structure functions $F_i^{\text{true}}(\tilde{x}_B, \tilde{Q}^2)$ requires unfolding, a procedure which is in general only possible in an iterative way and with reasonably chosen assumptions about the starting values. Moreover, the observed structure functions depend on the way in which the kinematic variables are measured. For example, if the momentum of the hadronic final state, p_X , could be measured, \tilde{x}_B and \tilde{Q}^2 would be known. In practice this will be difficult to achieve; however, any information about the hadronic final state could contribute to a narrowing down of the phase space available for photon emission, thereby reducing the size of radiative corrections.

The radiator functions are dominated by peaks in the angular distribution for the collinear radiation of photons from the initial state (ISR) or from the final state (FSR). At high energies, it is a good approximation to assume that photon radiation can be described by a simple rescaling of the lepton momentum, $l \rightarrow zl$ for ISR and $l' \rightarrow l'/z$ for FSR. The radiator function in the collinear approximation takes the simple, universal form

$$R_{\text{coll}} = \frac{\alpha}{2\pi} \log \frac{Q^2}{m_e^2} \left(\frac{1+z^2}{1-z} \right)_+ \quad (5)$$

so that the cross section is obtained from

$$d\sigma_{\text{ISR}} = \int \frac{dz}{z} R_{\text{coll}}(z) d\sigma_{\text{Born}}(l^\mu \rightarrow zl^\mu) \quad (6)$$

(and similarly for FSR). The potentially large logarithm $\log Q^2/m_e^2$ may reach the order of 10 % at large Q^2 .

As an example, we show numerical results for electron proton scattering at two typical sets of beam energies: $E_e = 5$ GeV with $E_p = 50$ GeV (left panel of figure 11) and $E_e = 30$ GeV with $E_p = 325$ GeV (right panel). The figures show the correction factor

$$r_c(y) = \frac{d\sigma/dy|_{O(\alpha)}}{d\sigma/dy|_{\text{Born}}} - 1 \quad (7)$$

where $y = Q^2/Q_{\text{max}}^2$, $Q_{\text{max}}^2 = x_B S$, $S = 2l \cdot P$. The different curves correspond to different ranges of x_B : at the lower center-of-mass energy (left panel of figure 11, from the bottom up): $0.1 < x_B < 0.4$, $10^{-2} < x_B < 10^{-1}$ and $10^{-3} < x_B < 10^{-2}$; at the higher center-of-mass energy (right panel, again from the bottom up): $0.1 < x_B < 0.4$, $10^{-2} < x_B < 10^{-1}$, $10^{-3} < x_B < 10^{-2}$, $10^{-4} < x_B < 10^{-3}$, and $10^{-5} < x_B < 10^{-4}$. The general features following from the preceding discussion are clearly visible: corrections are large at large y and small x_B , while corrections become negative at large x_B and small y .

Lacking a full Monte Carlo event simulation for scattering with heavy nuclei at present, we have studied the influence of a simple cut on the invariant mass of the hadronic final state. Imposing the condition $W_{\text{had}} > 1.4$ GeV would remove the elastic tail and the

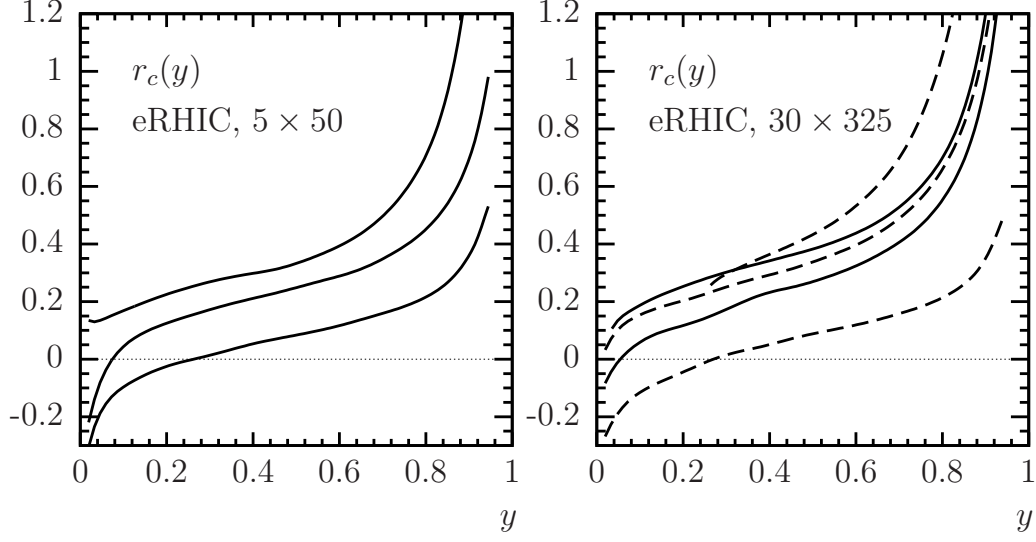


Figure 11: y -dependence of the leptonic radiative correction factor for electron proton scattering with different beam energies and in different x_B ranges. Left figure: $E_e = 5$ GeV, $E_p = 30$ GeV and the curves from the bottom up correspond to $0.1 < x_B < 0.4$, $10^{-2} < x_B < 10^{-1}$, $10^{-3} < x_B < 10^{-2}$; right figure: $E_e = 30$ GeV, $E_p = 325$ GeV and $0.1 < x_B < 0.4$, $10^{-2} < x_B < 10^{-1}$, $10^{-3} < x_B < 10^{-2}$, $10^{-4} < x_B < 10^{-3}$, $10^{-5} < x_B < 10^{-4}$ (full and dashed lines alternating for better visibility).

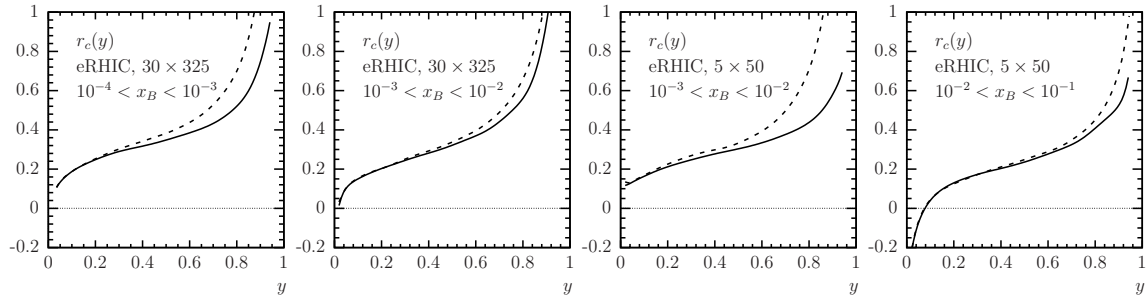


Figure 12: Influence of a cut on the mass of the hadronic final state on the leptonic radiative correction factor for a proton target in different x_B ranges and beam energies as indicated in the figures. Dashed curves are without a cut, full curves are obtained after a cut of $W_{\text{had}} > 1.4$ GeV.

contribution from low-lying resonances. A similar effect can be achieved cutting on $E - p_z$ from the Jacquet-Blondel method. The effect of such a naive cut is shown in figures 12. The reduction of the radiative corrections is considerable at largest y and at small x_B , but probably not yet sufficient at larger values of x_B . From similar studies for electron-nucleus scattering at HERA [5, 6, 2], one can expect to obtain a much stronger reduction of radiative corrections, if more refined prescriptions for the measurement of kinematic variables are found.

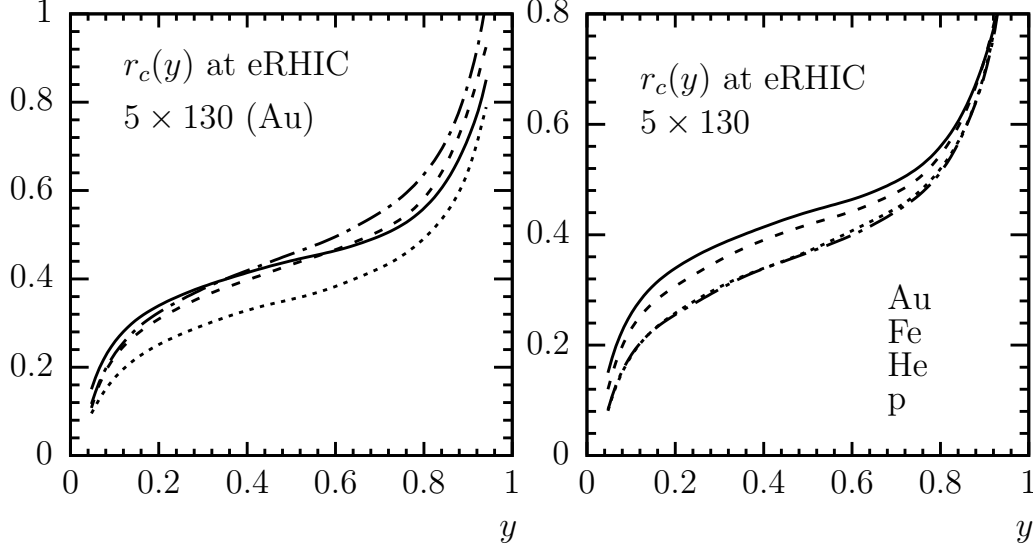


Figure 13: Left: Radiative corrections for electron scattering off a Au nucleus at 5×130 GeV² beam energies, $10^{-3} < x_B < 10^{-2}$, $Q^2 > 1$ GeV², $W_{\text{had}} > 1.4$ GeV with different models for nuclear PDFs: EPS09 (full curve), EPS08 (dash-dotted line), EKS98 (dashed line) and HKN (dotted line). Right: Radiative corrections for different nuclei with CTEQ61M PDFs modified by the EPS09 prescription. Beam energies and kinematic range as in the left figure. From the bottom up: proton, ⁴He, ⁵⁶Fe, ¹⁹⁷Au.

Since the determination of the true structure functions requires an iterative unfolding procedure, it is important to show that the radiative corrections do not depend too strongly on the assumed input structure functions. In figure 13a we show the correction factor $r_c(y)$ as defined above for the case of electron scattering off a ¹⁹⁷Au nucleus, assuming different parameterizations of parton distribution functions corrected for nuclear effects, as available in the literature [7, 8, 9, 10]. Although differences at the level of 10 % are visible, one can still observe a similar over-all behavior of radiative corrections. Finally, in figure 13b, we show results for scattering off different nuclei, again supporting the assumption that a common unfolding procedure would allow one to obtain the true structure functions.

Corrections due to the emission of photons from the hadrons, or quarks in the deep inelastic regime, require a careful separation into contributions which should be considered as a part of the hadron structure (leading to an electromagnetic contribution to scaling violations [11]) and contributions which can, in principle, be related to the observation of direct photons radiated from quarks. The interference of radiation from the lepton and the quark is small [5]. In certain phase space regions one may expect higher than one-photon corrections to be important. For example, soft-photon exponentiation will be necessary at small y and large x_B . The procedure is well-known and straightforward. Finally, multi-

photon radiation may become important at large y and small x_B . In this case, the collinear approximation is sufficient to reach a precision at the level of one percent [12].

1.3 Detector Design for eRHIC

The BNL design of an EIC allows for collisions at three interaction regions: one at IP-12 with a new dedicated EIC detector, and at IP-6 and IP-8 with the current RHIC detectors STAR and PHENIX. In the following first the design considerations for a dedicated EIC detector are described and then the capabilities of PHENIX and STAR for ep / eA collisions are discussed.

1.3.1 A dedicated EIC detector

Combining all the requirements described in section 1.1 and in the physics chapters before, a schematic view of the emerging dedicated eRHIC detector is shown in fig. 14. As already

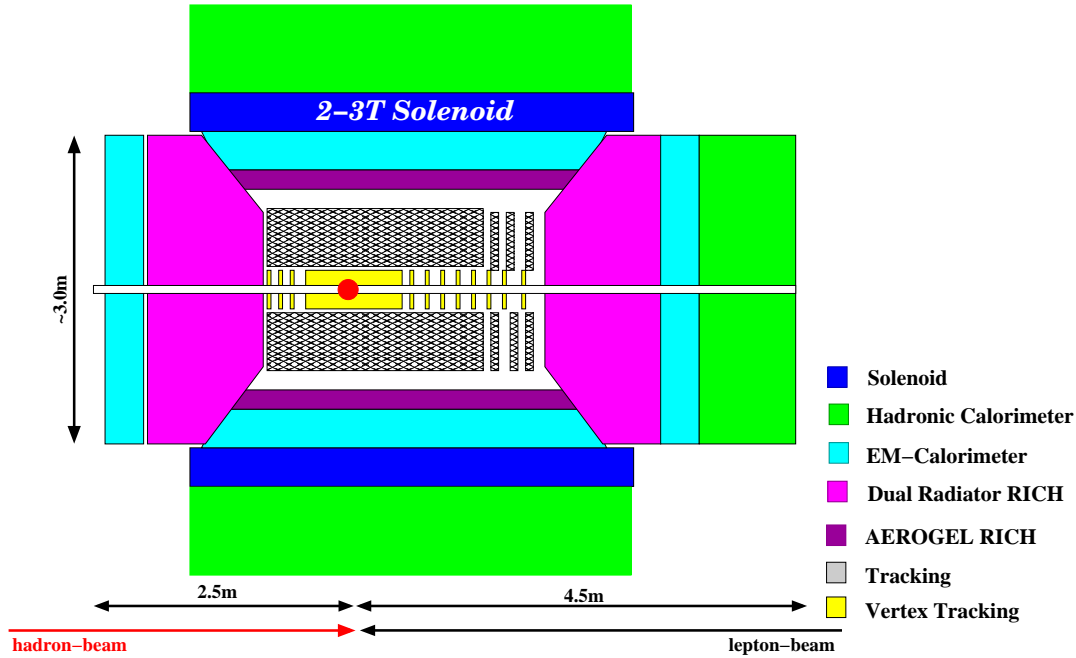


Figure 14: A schematic view of a dedicated EIC detector. Details of the GEANT-3 model can be found at https://wiki.bnl.gov/eic/index.php/Detector_Design.

discussed, it is important to have equal rapidity coverage for tracking and electromagnetic calorimetry. This will provide good electron identification and give better momentum and angular resolutions at low inelasticity y than with an electro-magnetic calorimeter alone.

The significant progress in the last decade in the development of Monolithic Active Pixel Sensors (MAPS), in which the active detector, analog signal shaping, and digital conversion take place in a single silicon chip (i.e. on a single substrate; see [13] and references therein), provides a unique opportunity for a μ -vertex detector for an eRHIC detector. These devices, built using CMOS technology, use an epitaxial layer as the active sensing element. Ionization deposited in the epitaxial layer is collected by N+ wells embedded in the epitaxial layer. The “pixel” pitch is determined by the location of the N wells so there is no need for

actual segmentation of the detector as is done with traditional hybrid pixel detectors. As a result, CMOS pixel detectors can be built with high segmentation, limited primarily by the space required for additional shaping and digital conversion elements. The key advantage of CMOS MAPS detectors is the reduced material required for the detector and the (on substrate) on-detector electronics. Such detectors have been fabricated and extensively tested (see e.g. [14]) with thicknesses of about $50\text{ }\mu\text{m}$, corresponding to 0.05% of a radiation length.

For tracking at larger radii there are several possibilities, which need to be investigated first through Monte Carlo studies for position resolution and material budget, and later through R&D and building prototypes. The two most prominent options for the barrel tracker are a TPC and a cylindrical GEM-Tracker. For large radii forward tracking GEM-Trackers are the most likely option. The projected rates for a luminosity of $10^{34}\text{ cm}^{-2}\text{ s}^{-1}$ range, depending on the center-of-mass energy, between 300 and 600 kHz, with an average of 6 to 8 charged tracks per event. These numbers do not impose strong constraints on the technology for a tracker.

Due to the momentum range to be covered the only solution for PID in the forward direction is a dual radiator RICH, combining either Aerogel with a gas radiator like C_4F_{10} or $\text{C}_4\text{F}_8\text{O}$ if C_4F_{10} is no longer available, or combining the gas radiator with a liquid radiator like C_6F_{14} .

In the barrel part of the detector several solutions are possible, as the momenta of the majority of the hadrons to be identified are between 0.5 GeV and 5 GeV. The technologies available in this momentum range are high resolution ToF detectors ($t \sim 10\text{ps}$), a DIRC or a proximity focusing Aerogel RICH.

For the electromagnetic calorimetry in the forward and backward direction a solution based on PbWO_4 crystals would be optimal. The advantages of such a calorimeter would be a small Molière radius of 2 cm and a factor of two better energy resolution and higher radiation hardness than, for example, lead-glass. To increase the separation of photons and π^0 s to high momenta and to improve the matching of charged tracks to the electromagnetic cluster, it would be an advantage to add, in front of all calorimetry, a high resolution preshower. We follow for the barrel part of the detector the concept of very compact electromagnetic calorimetry (CEMCal). A key feature is to have at least one preshower layer with 1–2 radiation lengths of tungsten and silicon strip layers (possibly with two spatial projections) to allow separation of single photons from π^0 to up $p_T \approx 50\text{ GeV}$, as well as enhanced electron-identification. A straw-man design could have silicon strips with $\Delta\eta = 0.0005$ and $\Delta\phi = 0.1$. The back section for full electromagnetic energy capture could be, for cost effectiveness and good uniformity, an accordion Lead-Scintillator Design, which would provide gain uniformity and the ability to calibrate the device. A tungsten- and silicon-strip-based preshower would also be a good solution for the forward and backward electromagnetic calorimetry.

To achieve the physics program as described in earlier sections it is extremely important to integrate the detector design into the interaction region design of the collider. As already described, particularly challenging is the detection of forward-going scattered protons from exclusive reactions, as well as of decay neutrons from the breakup of heavy ions in non-diffractive reactions. Previous experience of electron colliders (SLAC, KEK B-factories) and HERA, an electron-proton collider, indicated difficulties with synchrotron radiation coming from bending the electron beam close to the interaction region (IR). The newest large improvements in luminosity at KEK in Japan, by introducing crab cavities, show that colliding heavy ions or protons with electrons could be obtained without bending the

electrons close to the IR, but that it is possible to use the crossing angle between the two beams without losing luminosity. This is the path chosen in the eRHIC design: a 10 mrad crossing angle between the protons or heavy ions during collisions with electrons. This choice removes potential problems for the detector induced by synchrotron radiation. To obtain luminosities higher than $10^{34} \text{ cm}^{-2} \text{ s}^{-1}$, very strong focusing close to the IR is required to have the smallest beam sizes at the interaction point. A small beam size is only possible if the beam emittance is also very small. The focusing triplets are 4.5 meters away from the interaction point (IP). The strong focusing quadrupoles induce very large chromaticities. The current eRHIC design has its highest values of the amplitude betatron functions of the same size as the present operating conditions of the RHIC collider. In addition the design allows a correction of the first, second and third order chromaticities by using sextupoles at the triplets as well as 180 degrees away from the quadrupoles source (as shown in Fig. 15).

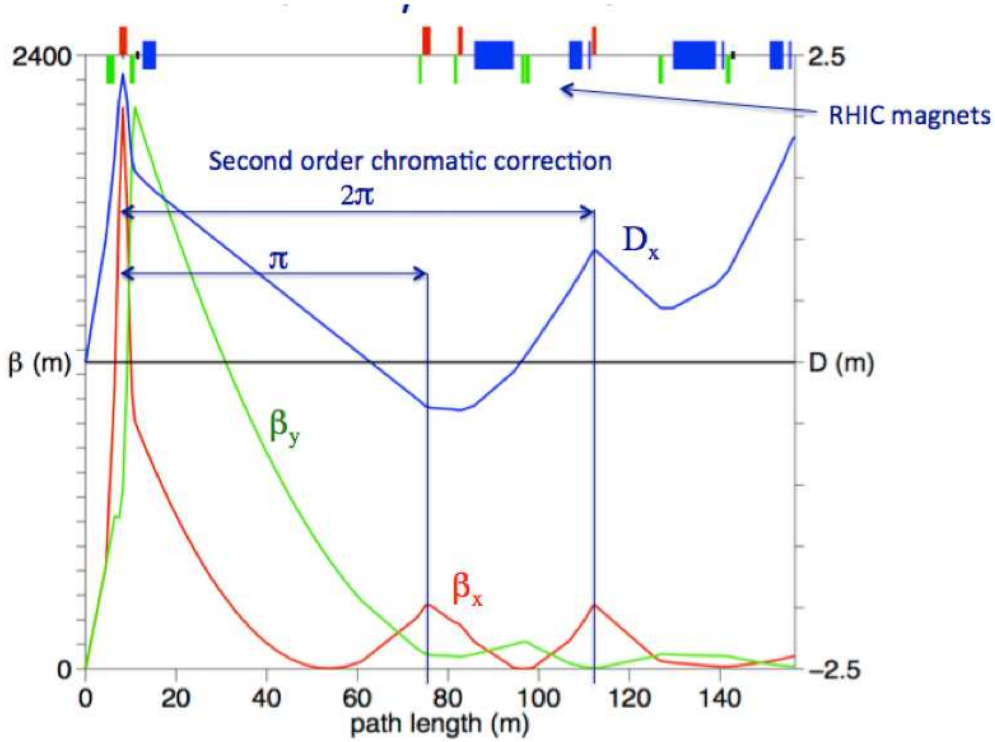


Figure 15: The Beta-function along the eRHIC hadron ring.

While the above accomplishes a small-emittance electron beam, the ions and protons need to be cooled by coherent electron cooling to have small emittance. The eRHIC interaction region design relies on the existence of small emittance beams with a longitudinal RMS of 5 cm, resulting in a $\beta^* = 5 \text{ cm}$. Strong focusing is obtained by three high-gradient quadrupole magnets using recent results from the LHC quadrupole magnet upgrade program (reaching gradients of 200 T/m at 120 mm aperture). To ensure the previously described requirements from physics are met, four major requirements need to be fulfilled: high luminosity (> 100 times that of HERA), the ability to detect neutrons, measurement of the scattered proton from exclusive reactions (i.e. DVCS), and the detection of low-momentum protons ($p \sim p_0/2.5$) from heavy-ion breakup. The eRHIC IR design fulfills all

these requirements: the first magnet in the high focusing quadrupole triplet is a combined function magnet producing a 4 mrad bending angle of the ion/proton beam (see Fig. 16). The 120 mm diameter aperture of the last quadrupole magnet allows detection of neutrons with a solid angle of ± 4 mrad, as well as the scattered proton from exclusive reactions, i.e. DVCS, up to a solid angle of ~ 9 mrad. The electrons are transported to the interaction point through the heavy ion/proton triplets, seeing zero magnetic field as shown in Fig. 16.

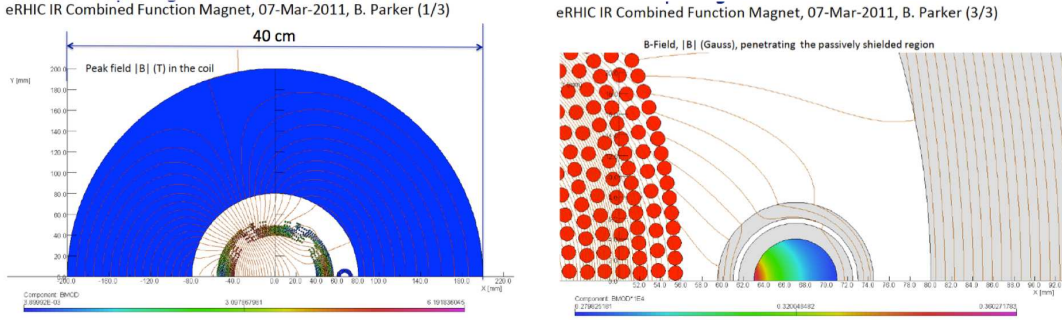


Figure 16: Combined-function magnet of the hadron beam high focusing quadrupole triplet.

Figure 17 shows the current eRHIC interaction region design in the direction of the outgoing hadron beam. The other side of the IR is mirror symmetric for the incoming hadron beam. For the outgoing lepton beam we are currently investigating how to best integrate a low scattering-angle lepton tagger. Such a tagger is critical for any low Q^2 physics, like elastic J/ψ production in eA collisions (see section ??).

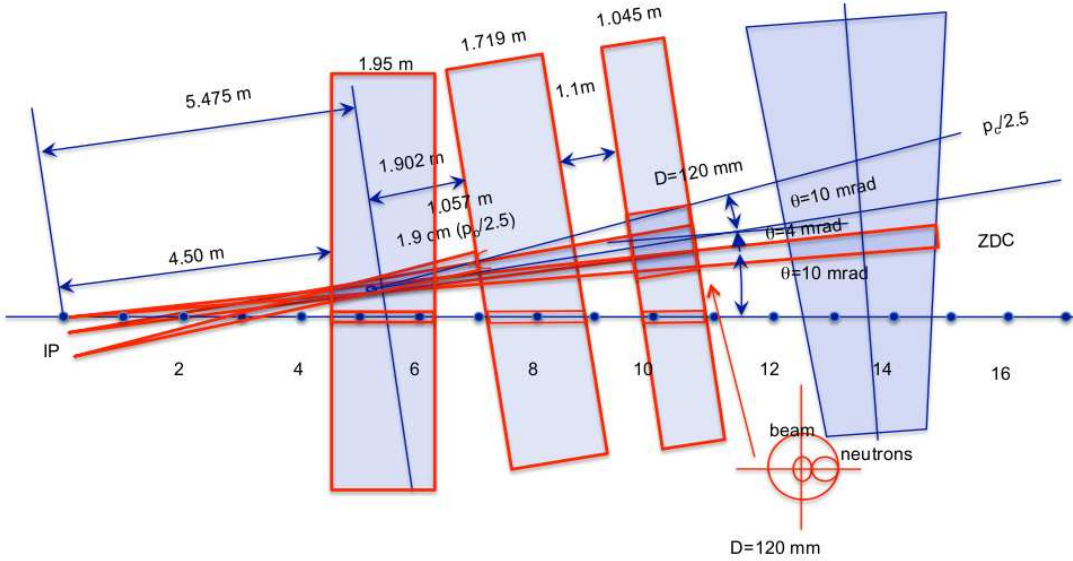


Figure 17: Schematic view of the eRHIC interaction region design in the direction of the outgoing hadron beam.

The scattered proton from DVCS events were tracked through this design and beam optics using HECTOR [15]. The DVCS events have been generated with MILOU, a MC

dedicated for DVCS [16]. From fig. 18 it is clear that protons from DVCS events can be measured in ‘Roman Pots’ after the high-focusing quadrupole triplet with a high detection efficiency for hadron beam energies starting from 100 GeV (as example are shown the results for 50 GeV and 250 GeV). More studies are needed to determine the momentum and angular resolution that can be achieved depending on the ‘Roman Pot’ design.

As pointed out previously, equally challenging is the detection of the breakup neutrons from heavy ions to veto incoherent events. The nuclear breakup of Au nuclei depending on the excitation energy E^* was simulated using the Monte Carlo generator GEMINI++ [17] and SMM [18]. The MC simulation showed that whenever the nucleus breaks up there will be at least one neutron emitted. At very low excitation energies there is the possibility that only a photon is emitted, while the nucleus remains intact. The possibility of detecting these photons still needs to be investigated. Figure 19 shows the angular distribution of the breakup neutrons for three different excitation energies. The aperture of 120 mm diameter of the last quadrupole magnet allows detection of neutrons with a solid angle of ± 4 mrad, which is indicated by the simulations to be sufficient.

Figure 20 shows the detection inefficiency for these neutrons for three different excitation energies as function of the maximal aperture of the last magnet. For apertures discussed for the IR design the inefficiencies are 10^{-2} or much lower for all excitation energies. This assumes a 100%-efficient zero degree calorimeter (ZDC). The critical question is: to suppress incoherent events at high t in eA collisions, can the detection inefficiencies be controlled on the 10^{-3} to the 10^{-4} level?

There are many detector, interaction region and machine parameters still to be worked out in detail, but one of the hardest questions for an EIC will be to estimate the limiting factors for the systematic uncertainties. Due to the high luminosity, many inclusive and semi-inclusive physics observables will be systematics-limited after relatively short time of data taking, assuming a 50% operations efficiency. This requires great care to be taken to consider the possible systematic limitations from the beginning and to integrate solutions to minimize them into the design. Only some of the possible limiting systematic effects that will need to be addressed with great care in the design are listed here. Their impact on key physics observables still needs to be studied.

- Absolute luminosity measurements between different beam energy combinations. This is extremely important for measurements like the structure function F_L .
- Relative luminosity measurements between bunches with different bunch helicities, i.e. $++$, $--$, $-+$ and $+-$. Here it will be important to investigate whether Bremsstrahlung can be used for this measurement, as the Bremsstrahlung cross section has a term that is dependent on polarization.
- The measurements of the absolute hadron and electron beam polarization. To date the best precision in the measurement of lepton beam polarization at high energies in a collider was obtained during HERA-I running with 1.6% [19]. At RHIC the till today best hadron polarization measurement achieved is $\sim 5\%$ [20, 21, 22] for a polarized proton beam. For high energy polarized ^3He beams first R&D is needed to determine how to measure an absolute polarization.

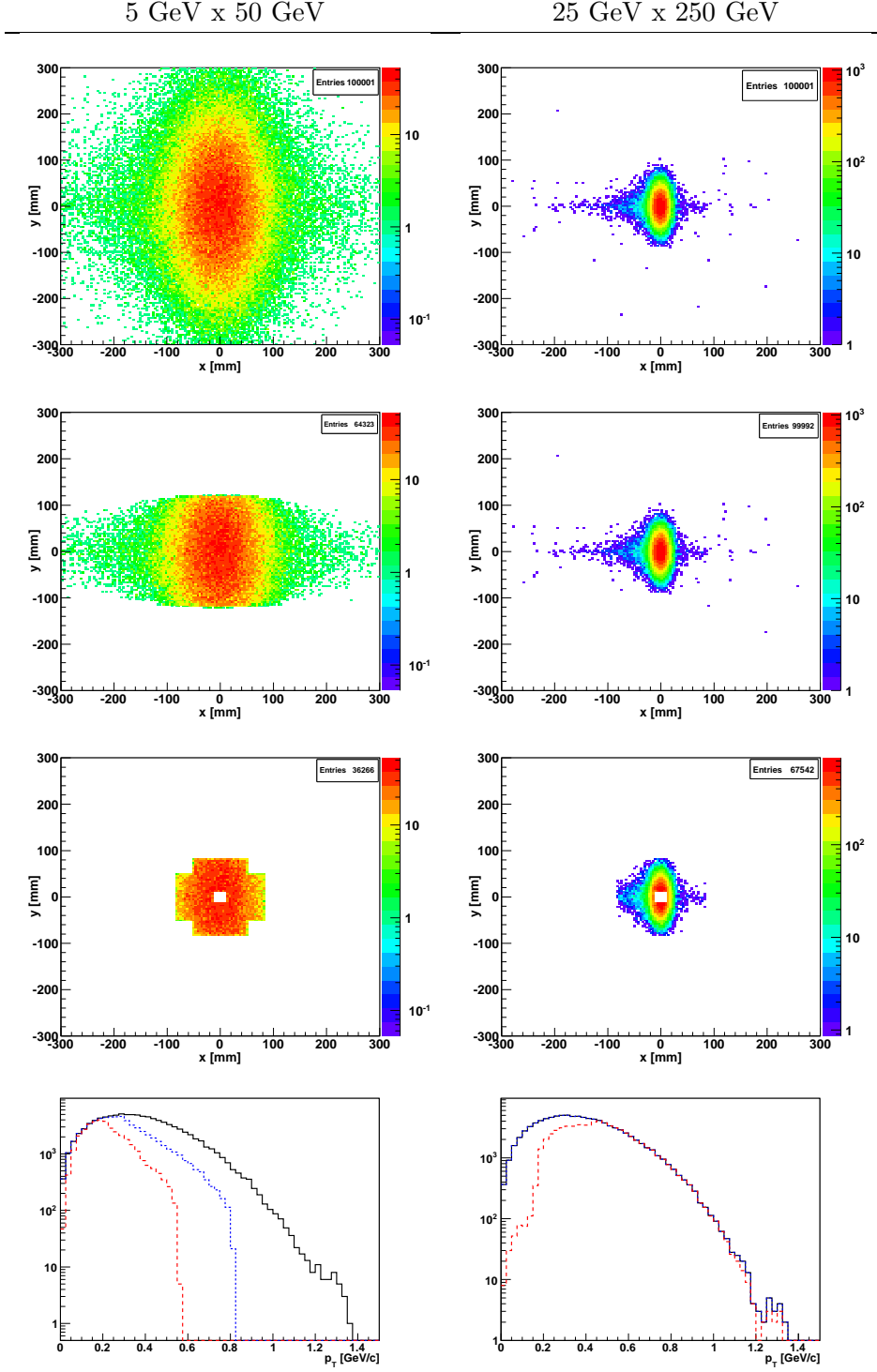


Figure 18: Row-1: Spatial distribution of the scattered protons from DVCS events at 20m from the IP for 2 different beam energy combinations. Row-2: As Row-1, applying the aperture limitations due to the magnets. Row-3: As Row-2, applying the limitations due to the 10σ beam clearance and the acceptance of 'Roman Pots' as currently used by pp2pp at STAR. Row-4: Comparison of the p_T spectrum of generated protons (black), those accepted by the quadrupole aperture (blue) and those detected in the 'Roman Pots' (red).

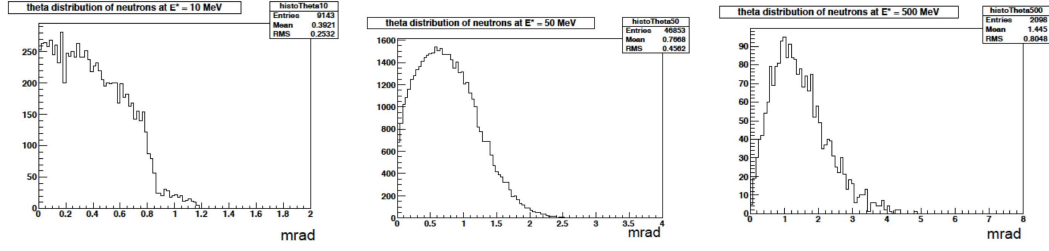


Figure 19: The angular distribution of neutrons from the breakup of a Au nucleus depending on the excitation energy.

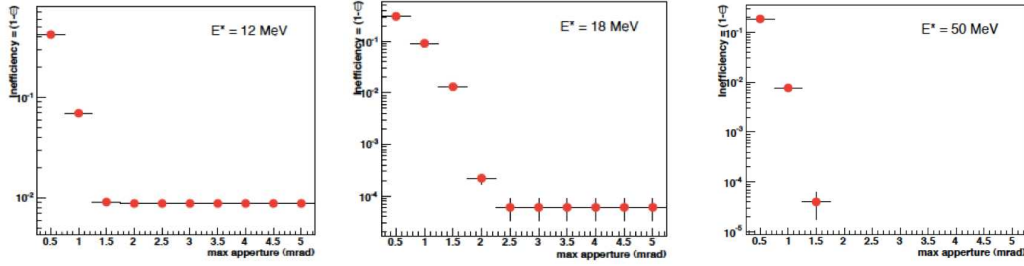


Figure 20: The inefficiency to detect the neutrons from the breakup of a Au-nucleus as function of the maximal aperture of the last magnet for different excitation energies.

1.3.2 ePHENIX

PHENIX is one of the two large dedicated RHIC detectors, located at IP-8. The PHENIX detector consists of the two Muon spectrometer arms and the two central arms sitting in a X tesla solenoid. Over the years the detector has been upgraded to the configuration shown in fig. 21. Figure 21 and the upper plot of fig. 22 show clearly that PHENIX in its current

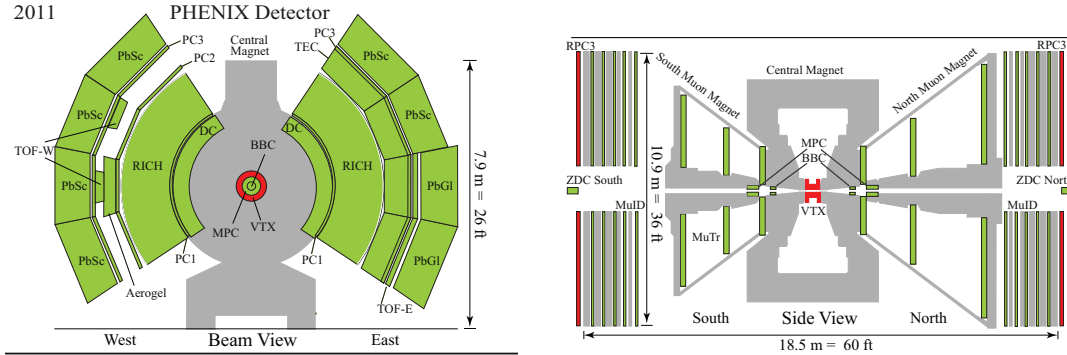


Figure 21: A schematic view of the current (2011) configuration of the PHENIX detector.

configuration has only a very small acceptance ($|\eta| < 0.35$) for the scattered lepton. This makes the current PHENIX detector basically not usable for DIS physics.

For the RHIC decadal plan covering the period 2010 - 2020, PHENIX has proposed a major upgrade of the current detector [23]. The decadal plan outlines an exciting program

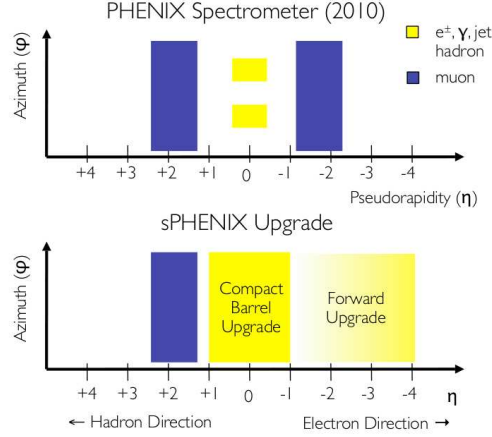


Figure 22: Rapidity coverage of the current PHENIX detector compared to the strawman new PHENIX detector. The central barrel detector covers $|\eta| < 1.0$; the forward detector has tracking coverage for $-4 < \eta < -1$, with full ECal and HCal coverage for $-4.0 < \eta < -2.0$ - (-1.5) with the exact range dependent on the final design configuration

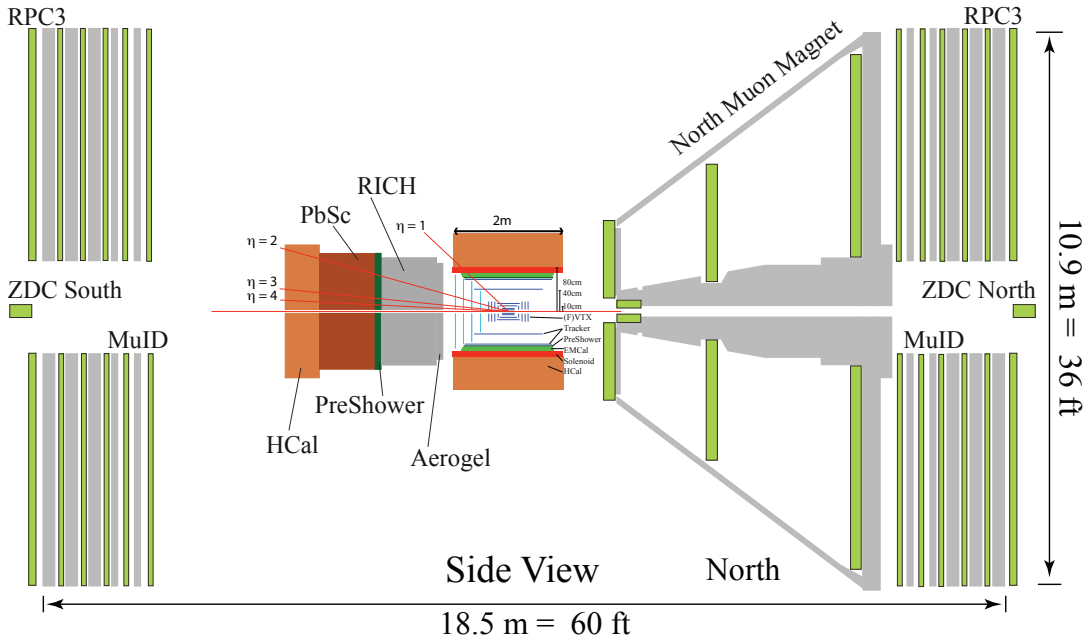


Figure 23: Schematic drawing of the new PHENIX detector.

in heavy ion and spin physics in polarized pp collisions, focused on an investigation of the interplay between perturbative and nonperturbative physics in QCD and on the relative importance of strong and weak coupling. The physics aims have been translated into an extensive set of required physics observables to answer the key scientific questions, leading to the design of the new PHENIX detector. The upgrade plan involves replacing the PHENIX central magnet with a new compact solenoid. The limited aperture provided by the outer central arm detectors would be replaced with a compact EMCal and a Hadronic Calorimeter covering two units in pseudorapidity and full azimuth, complemented by the existing VTX and FVTX inner silicon tracking. Two additional tracking layers would be added. We highlight that the large acceptance and excellent detector capability is combined with high rate and bandwidth. The limited forward coverage of the current PHENIX detector does not allow us to adequately address the questions driving the nucleon structure and cold nuclear matter community, nor does it provide any capabilities for e+p or e+A collisions. Hence, we are considering an upgrade where one muon arm would be replaced by a new large-acceptance forward spectrometer with excellent PID for hadrons, electrons, and photons and full jet reconstruction capability. The modified detector layout is shown schematically in fig. 23. The increase in overall acceptance is shown in the lower part of fig. 22. The new compact barrel component at midrapidity is designed for excellent jet reconstruction and PID for photons, electrons, and π^0 in p+p, proton-nucleus, through central nucleus-nucleus collisions. The forward upgrade design is driven by nucleon structure physics and cold nuclear matter physics. Such a forward spectrometer added to PHENIX would not only allow measurements of the single spin asymmetry at forward rapidity to test the QCD prediction that the Sivers function in Drell-Yan and SIDIS is opposite, but would also allow the unique possibility to detect the scattered lepton in e+p/e+A collisions in the era of an eRHIC to virtualities $Q^2 > 0.1 \text{ GeV}^2$. To realize these physics goals it is necessary to upgrade significantly the current PHENIX detector to a detector with high acceptance at forward rapidity $1 < \eta < 4.0$.

The strawman design for the central barrel has already been described. The forward detectors of the strawman design consist of a RICH, a preshower, an EMCal, an HCal, and additional tracking detectors to provide good momentum definition of the particles going forward. This combination of detectors is motivated by both Drell-Yan and e+p/e+A physics to emphasize the detection of electrons with high efficiency and purity.

It must be stressed again that the PHENIX detector upgrades as discussed above are driven by p+p, p+A, A+A physics. But comparing the requirements for the physics program at an EIC as described in section 1.1 it becomes clear that this detector upgrade also provides opportunities to carry out an e+p and e+A physics program, referred to as ePHENIX. The upgraded PHENIX is well suited for

- Inclusive e+p physics to measure polarized and unpolarized structure functions.
- Inclusive e+A physics to measure unpolarized structure functions and derive nuclear parton distribution functions (nPDFs).
- e+p / e+A physics involving charm and bottom
- Elastic diffractive physics, i.e. elastic vector meson production and deeply virtual Compton scattering. These measurements require the addition of ‘Roman pot’ detectors.

nearly independent of the center-of-mass energy and lepton and hadron beam combination. Unfortunately due to the limited PID capabilities of the ePHENIX most of the SIDIS physics program for an EIC will not be possible.

There are still several open question on the detailed performance of the upgraded PHENIX detector in ep / eA collisions, which need to be studied in the next month. Some examples are given below. Of course, some of these concerns can easily be solved by addressing them by design changes.

- How can ePHENIX be integrated in the current IR design of eRHIC?
- What does the current material budget do to the momentum and angular resolution of the scattered lepton?
- Does the current compact solenoid provide enough bending power to achieve sufficient momentum resolution for the scattered lepton at low Q^2 ?
- How can a luminosity measurement for ep/eA collisions be integrated in the design?
- Are the currently planned electromagnetic calorimeter designs suited in energy resolution to separate leptons from hadrons via E/p , and to get the required resolution for the DVCS photon?

1.3.3 eSTAR

STAR is the other of the two large dedicated RHIC detectors, located at IP-6. Figure 24 shows STAR in the configuration anticipated in 2014.

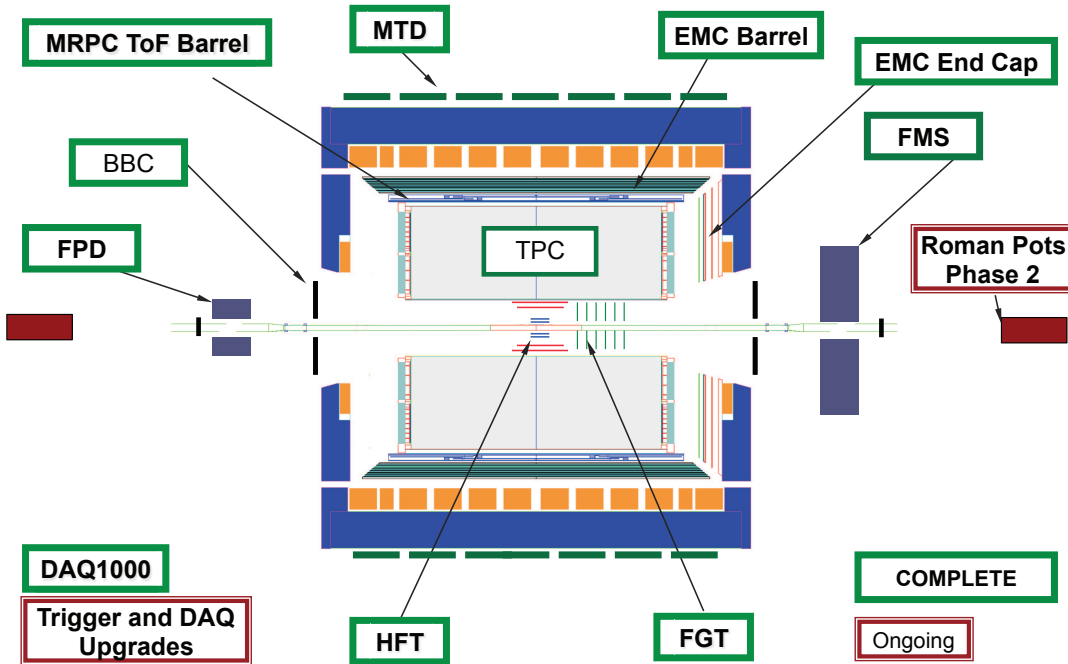


Figure 24: Schematic drawing of the STAR detector in 2014.

The unique strength of STAR (solenoidal tracker at RHIC) [24] is its large, uniform acceptance capable of measuring and identifying a substantial fraction of the particles produced in heavy ion collisions. The heart of STAR is its main tracking device: a TPC, covering full azimuthal angle and ± 1.5 units of pseudo-rapidity. A dE/dx resolution of $\sim 8\%$ can be achieved by requiring the tracks of charged particles to have at least 20 out of a maximum of 45 hits in the TPC. Detailed descriptions of the TPC and its electronics system have been presented in [25, 26]. The TPC sits in a 0.5 tesla solenoid, surrounded by electromagnetic calorimetry (EMC Barrel, EMC End Cap, FMS) covering $-1 < \eta < 4$, muon identification (MTD) covering $-1 < \eta < 1$ and a high-resolution time of flight system (MRPC ToF Barrel) covering $-1 < \eta < 1$. The tracking in STAR will be further improved by 2014 by adding a forward GEM tracker (FGT) covering $1 < \eta < 2$ and a high-resolution silicon detector (HFT) covering $-1 < \eta < 1$. The HFT gives the possibility to separate events with charmed mesons from those with beauty mesons through the detection of the displaced vertex for charmed mesons. Identification in the lepton sector will be enhanced with the Muon Telescope Detector (MTD), which will tag muons for $-1 < \eta < 1$. This will enable dilepton studies in the $\mu - \mu$ and $e - \mu$ channels, with a focus on separating the Upsilon states and constraining charm backgrounds to the thermal continuum in intermediate mass dileptons. Another unique feature of STAR is the ‘Roman Pots’ around the main detector; their main focus is to detect protons from elastic diffractive events in pp collisions.

In addition to large coverage in tracking and electromagnetic calorimetry, STAR has good particle identification capabilities. For stable charged hadrons, the TPC provides π/K ($\pi+K/p$) identification to $p_T \sim 0.7$ (1.1) GeV/c by the measurement of ionization energy loss (dE/dx). The STAR PID capability is further enhanced by the TOF system with a time resolution of < 100 ps, which is able to identify π/K ($\pi+K/p$) to $p_T \sim 1.6$ (3.0) GeV/c, as demonstrated in the left panel of fig. 25. In addition, with the relativistic rise

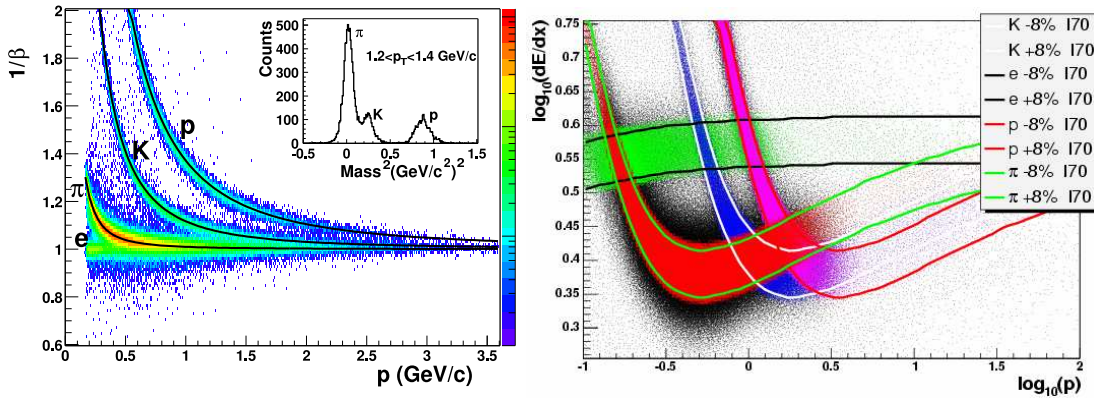


Figure 25: Left: $1/\beta$ vs. momentum for π^\pm , K^\pm , and $(p\bar{p})$ from 200 GeV d+Au collisions. Separation between pions and kaons (kaons and protons) is achieved up to $p_T \sim 1.6$ (3.0) GeV/c. The insert shows $m^2 = p^2(1/\beta^2 - 1)$ for $1.2 < p_T < 1.4$ GeV/c. Right: Distribution of $\log_{10}(dE/dx)$ as a function of $\log_{10}(p)$ for electrons, pions, kaons and (anti-)protons. The units of dE/dx and momentum (p) are keV/cm and GeV/c, respectively. The color bands denote the $\pm 1\sigma$ dE/dx resolution.

of dE/dx from charged hadrons traversing the TPC at intermediate/high p_T (> 3 GeV/c) and diminished yields of electrons and kaons at this p_T range, pions and protons can be identified up to very high p_T (~ 10 GeV/c) in p+p, p+A and A+A collisions (see right panel fig. 25).

STAR has, like PHENIX, provided a decadal plan [27] outlining the physics program for pp, dA and AA collisions in the next 10 years. Contrary to PHENIX, the STAR upgrade plans are much more moderate and focus on forward rapidity ($2 < |\eta| < 4$). One the side of the STAR detector at which the FMS is situated, the plan is to improve charged particle tracking by adding more tracking planes to the FGT to cover rapidities $2.5 < \eta < 4$. To improve lepton/hadron and γ/π^0 discrimination, as well as baryon/meson separation, a RICH detector and a preshower detector will be added in front of the FMS. The addition of a hadronic calorimeter behind the FMS will further improve the lepton/hadron separation, as well give the possibility of measuring the energy due to neutral particles in jet reconstruction. The motivation for this upgrade is, like in the case of the PHENIX forward upgrade, transverse spin physics in pp collisions (Sivers asymmetry in Drell Yan) and the study of cold nuclear matter, i.e. parton saturation at small x .

The upgrade in rapidity $-4 < |\eta| < -1$ is driven solely toward improving the detection capabilities of STAR for the scattered lepton in ep/eA collisions during the era of eRHIC. Currently proposals include the addition of tracking and electromagnetic calorimetry as well as an additional ToF for PID. For tracking, it is proposed to combine high-resolution with electron identification by for example integrating a Cerenkov detector in the tracking detector.

Combining all these upgrades fig. 26 shows that STAR will have very good acceptance for both the scattered lepton and for the hadrons produced by the current jet at the first stage of eRHIC, with 5 GeV electron beams colliding with proton beams with energies as high as 325 GeV. From these figures it is also obvious that the upgrade at negative rapidity is essential to provide good coverage for the scattered lepton below Q^2 of 10 GeV^2 .

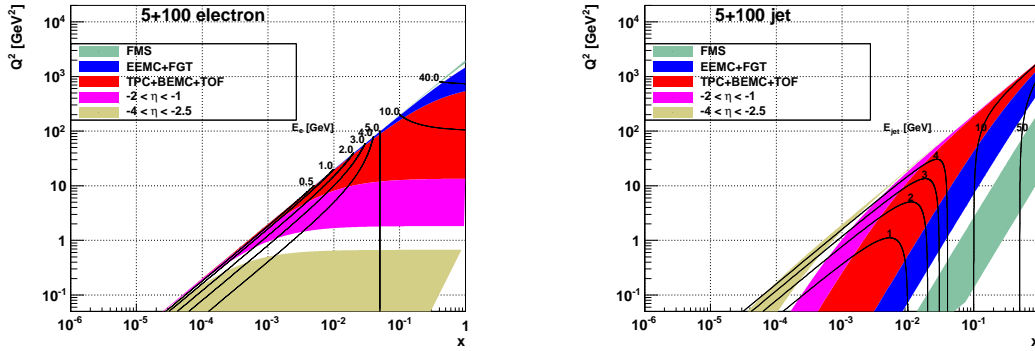


Figure 26: Kinematic coverage of the STAR detector in the (x, Q^2) plane. Left: electron. Right: struck quark. The electron beam energy is 5 GeV, and the nucleus beam energy is 100 GeV/u. Lines of constant laboratory energy of the electron and the struck quark are shown.

The list of questions which need to be answered is very similar to that listed in the ePHENIX section, and many further detailed simulations must be performed to understand in detail the performance of STAR for ep/eA collisions. However from the first studies it is clear that eSTAR will be able to make key measurements such as:

- Inclusive e+p physics to measure polarized and unpolarized structure functions.
- Inclusive e+A physics to measure unpolarized structure functions and derive nuclear parton distribution functions (nPDFs).

- Elastic diffractive physics, i.e. elastic vector meson production and deeply virtual Compton scattering. Here the great advantage is that eSTAR already possesses ‘Roman pot’ detectors.
- The good particle ID capabilities also open the possibility of studying many of the semi-inclusive observables in ep/eA collisions, i.e. to do a flavour separation of the quark polarizations to understand both the helicity structure and the transverse spin structure (via Sivers and Collins functions) of the proton.

1.4 Detector Design for MEIC/ELIC

The Jefferson Lab design of an EIC is based on a novel figure-8 ring-ring design optimized for polarization preservation. The initial version of this EIC is termed the Medium-Energy EIC, or MEIC, which is upgradable to a higher-energy version termed Electron Ion Collider, or ELIC. The MEIC/ELIC will have minimal impact on continued operation of the Jefferson Lab (JLab) 12 GeV fixed-target program.

The ring-ring design of the MEIC/ELIC allows simultaneous operation at high luminosity of multiple detectors located at different interaction points (IPs). Due to the nature of the figure-8, four IPs are foreseen with different functions. The MEIC detector/interaction region has concentrated on *maximizing acceptance* for deep exclusive processes and processes associated with very-forward going particles, which are the most challenging from detector point of view. This section will describe the baseline full-acceptance detector in more detail, where it is understood that the various MEIC/ELIC interaction points can house detectors employing different technologies and having slightly different physics focus.

Given that the detailed design of various subsystems does not have to be frozen for another decade or so, and dedicated pre-R&D projects are only now under way, the focus of the JLab effort has been on formulating requirements, identifying and addressing critical design issues, and integrating the detector with the interaction region of the accelerator. A tentative detector configuration with estimates based on realistic projections has been adopted, however, to provide users with input for simulations.

1.4.1 The Medium-energy EIC (MEIC)

The current effort is geared towards the MEIC, for which the guiding principle has been based upon science motivation and design choices close to present state-of-the-art whenever possible. The exception to the latter is the ion beam properties, which have been established for electron-positron colliders but fundamentally depend on electron cooling for proton/ion beams. The fundamental choice for the MEIC design has been to assume short bunches, each carrying a small charge, and to achieve the requirements for the proton beam quality assume extrapolations from conventional electron cooling that have been successfully employed at Fermilab, albeit at modest proton energies. Extending this technology may be incremental, rather than transformational in nature.

While ELIC would have a circumference of about 3 km, and support proton energies in excess of 250 GeV (as well as heavy ions of more than 100 GeV/A), and electrons post-accelerated up to about 20 GeV, the MEIC would be somewhat smaller than the 1.4 km of the CEBAF accelerator, from which it would inject electron or positron beams between 3 and 11 GeV. The maximum proton energy would be around 100 GeV (or 40 GeV/A for heavy ions), but the often quoted design point for which performance parameters are being worked out in detail, is 60 GeV. The choice of a mid-range energy for these studies

is primarily based on two considerations. On the accelerator side, a proton energy of 60 GeV is a somewhat more conservative value for which one could anticipate the performance projections for the electron cooling to become valid at an early stage of operations. On the physics side, a range of measurements, for instance related to the 3D structure of the nucleon, place strong demands on the resolution in t and the luminosity at modest values of proton energy, corresponding to $s \sim 2000 \text{ GeV}^2$.

To further illustrate the importance of a mid-range energy for detailed imaging studies through exclusive reactions, we come back to the kinematics associated with these processes, but for a cut in $Q^2 > 10 \text{ GeV}^2$, a likely must for the valid partonic interpretation of such studies. If one implies a $Q^2 > 10 \text{ GeV}^2$ cutoff in such exclusive processes, the kinematic patterns of earlier Fig. 6 drastically change. The upper panels of Fig. 27 shows how the momentum distribution of mesons associated with exclusive pseudoscalar meson production change with lepton and proton energy. Compared to Fig. 6 the peak in the forward-ion direction has disappeared completely. Lower lepton energies also push towards lower hadron momenta in the central-angle region, and thus reduced Particle Identification requirements. The bottom panels of Fig. 27 show one of the most challenging constraints on the detector and interaction region design for exclusive reactions from the need for detection of the exclusive hadronic state remaining in the exclusive process. The figures show the direct correlation between t and proton energy, scaling like $1/E_p$, and shows the remaining baryonic state goes very much in the forward-ion direction, but far less so (and with lower momenta) for lower proton energies, which are thus much easier to peel off from any beam-stay-clear area. Even more, assuming a fixed resolution in t , there are obvious benefits of lower proton energies for imaging. Of course, any high-energy ELIC would in turn greatly benefit from the experience gained from the construction and operation of the MEIC.

While maintaining a future upgrade path to the high-energy ELIC is important and always folded into the MEIC design, emphasis has been placed on ensuring that ELIC will not simply supersede the MEIC, but rather provide a complementary capability. The MEIC is thus designed to excel in the kinematic range that it will cover (i.e., on one hand having an overlap with JLab 12 GeV, and on the other with HERA data with $y < 0.3$). Overlap in science goals is in part achieved by various accelerator features. Perhaps one of the most prominent is the figure-8 shape, which could allow storage of polarized deuterium beams. By tagging the spectator proton in the small-angle ion spectrometer (discussed below), this will allow to carry out measurements on quasi-free (polarized) neutrons. A high luminosity over a broad kinematic range will make it possible to accumulate sufficient statistics for multiple beam energy settings. The capability to vary the beam energies is essential for some measurements (e.g., F_L), but also makes it possible to optimize the data taking by reducing reliance on data taken at extreme values of y , where the systematic uncertainties grow. This can be achieved by having a lepton beam energy that can be varied continuously, and a series of closely spaced discrete ion beam energies. In the MEIC, the latter can be accomplished by changing the number of stored ion bunches by one, and the bunch separation distance accordingly - a scheme facilitated by the high bunch repetition frequency. Independently varying beam energies also makes it possible to choose the most suitable lab kinematics at a certain value of s , potentially improving acceptance, resolution, and particle identification for the reaction of interest (see also Fig. 27).

Having small, short ion bunches with a high bunch repetition frequency also facilitates the use of SRF crab crossing cavities, which were originally developed for KEKB to allow beams collide at an angle without significant loss of luminosity. In the context of an EIC, these were pioneered in the ELIC design, and the possibility of creating a significant crossing

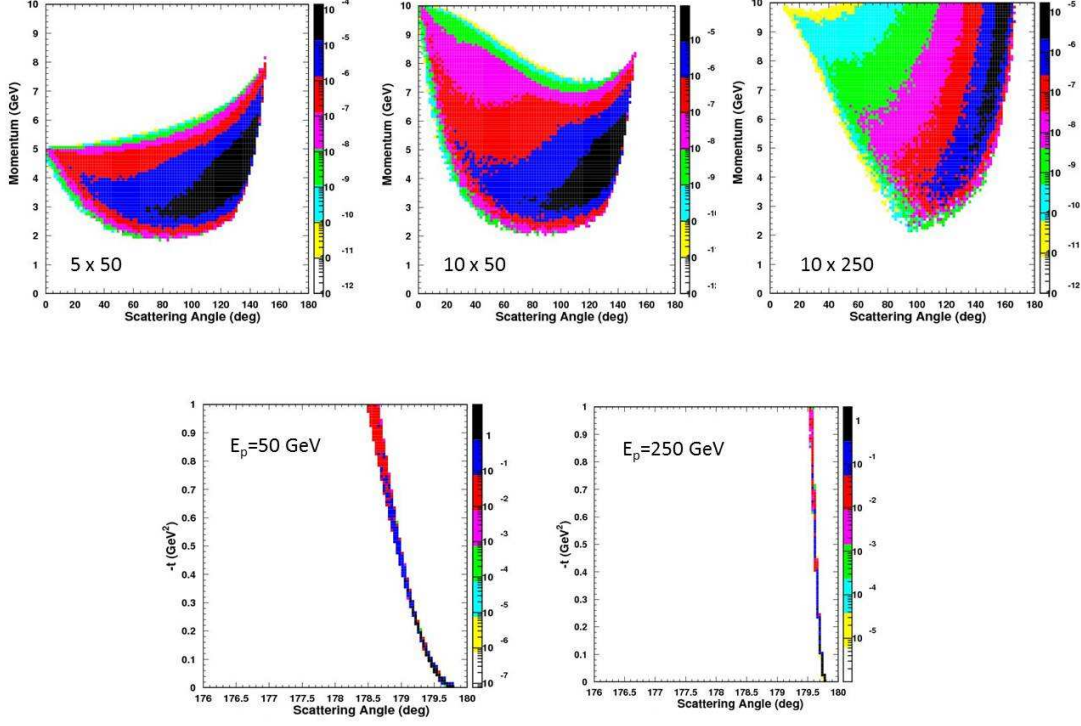


Figure 27: The momentum distribution of the exclusive hadronic final state as a function of the scattering angle for three different center of mass energies, $\sqrt{s}=31.6, 44.7, 100$ GeV (upper three panels), and the t distribution as a function of scattering angle of the recoiling baryon in exclusive reactions for proton beam energies $E_p=50$ GeV and 250 GeV (lower two panels). A cut of $Q^2 > 10$ GeV² is applied to select the kinematic range of interest for exclusive processes as discussed in section XYZ. For lower center of mass energies, the momentum distribution tends towards more central scattering angles and covers lower momenta. The angle of the recoiling hadronic system is directly and inversely correlated with the proton energy as described in section XYZ. It thus decreases with increasing proton energy. For instance, as shown here, the baryon scattering angle ranges to about 1-2° at a proton energy of 50 GeV and is reduced to one fifth of that as the proton energy increases to 250 GeV.

angle (at least 50 mrad) became early on a key feature of the small-angle detection for the MEIC (see section 1.4.6).

1.4.2 Detector Placement and Backgrounds

The figure-8 ring can support two IPs per straight section, one of which will be a “high-luminosity” IP with the full crossing angle. In order to minimize backgrounds, the two high-luminosity IPs will be located close to where the ion beam exits the arc, and far away from the arc where the lepton beam exits. The latter helps to decrease synchrotron radiation (and the secondary neutron flux) at the IP, which is anyway already reduced due to the use of crab crossing (with the ion beam, not the electron beam, making the horizontal bend correction). The synchrotron background is reduced even further by lowering the strength of the last arc dipoles. The short distance between the ion arc and IP suppresses detector backgrounds from interactions of the beam with residual gas in the beam pipe by providing a smaller “target” with line-of-sight to the detector. A shorter section of the beamline is also easier to bake and keep at ultra-high vacuum. A comparison with HERA, also taking into account the lower $p-p$ (and $p-A$) cross section and lower hadron multiplicity at the 100 GeV, suggests that the hadronic background will be about an order of magnitude lower in the MEIC at comparable vacuum and ion beam current, leaving a lot of headroom to increase the latter. Due to the bends associated with the horizontal crossing, the secondary IPs on each straight section will not have a line-of-sight along the full straight section, but there this is less of an issue since they are intended to either have diagnostics equipment (*e.g.*, polarimetry), or special detectors which are less sensitive to backgrounds or intended to operate at lower beam currents.

1.4.3 Detector and Interaction Region Layout

A global outline of the fully integrated MEIC detector and interaction region is given in Fig. 28. We will in the subsequent subsections go in more detail over the central detector region, defined as the region of the detectors operating within the solenoid, the electron and ion endcaps, and the strategy to accomplish a full-acceptance detector. The latter has two ingredients, a relatively simple approach to incorporate low- Q^2 electron detection and a more challenging solution to measure forward and ultra-forward (in the ion direction) going hadronic or nuclear fragments. Here, we make critical use of various ingredients of the MEIC detector/interaction region design: i) the 50 mrad crossing angle; ii) the range of proton energies; iii) a small 1-2 Tm dipole field to allow measurement down to 0.5° before the ion final focusing magnets; iv) ion final focusing magnets with apertures sufficient for particles with angles up to at least 0.5° ; and v) a large 20 Tm dipole field much more downstream to peel off spectator particle and allow for very small-angle detection.

The strategy will be that various detector elements, amongst which zero degree calorimeters for neutron detection and various small-angle detectors, will be placed in the region between the ion final focusing quads and the 20 Tm dipole field, and also beyond this 20 Tm dipole field. This then results in an essentially 100% full acceptance detector. The electron beam traverses the center region of the solenoid, while the proton/ion beam traverses at the crab crossing angle. This choice minimizes any electron steering and synchrotron radiation. Note that the 50 mr crab crossing angle also facilitates the small-diameter electron final focusing quads to be moved in to 3.5 meter distance of the interaction point. The lower electron beam energies and hence lower-field requirements for the electron beam allows

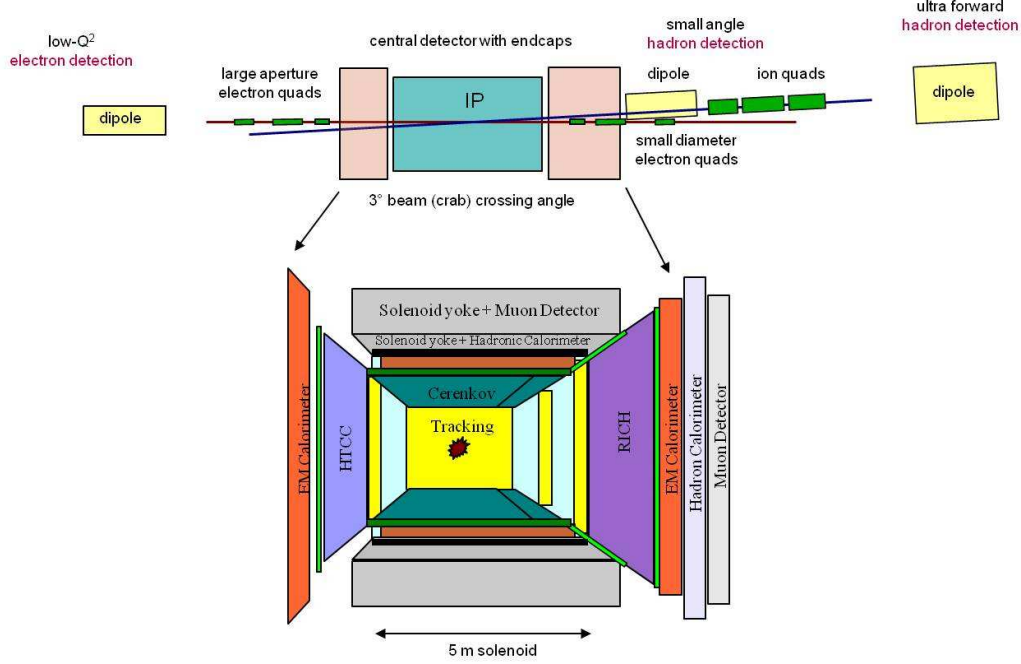


Figure 28: Interaction region and central detector layout, and its placement in the general integrated detector and interaction region. The central detector includes endcaps in both the electron and ion direction.

the construction of relatively small-sized quadrupoles, much simplifying the electron optics design.

1.4.4 Central Detector

To fulfill the requirement of hermeticity, the central detector will be build around a solenoid magnet (with a length of about 5 m). Due to the asymmetric beam energies, the interaction point (IP) will be slightly offset towards the electron side (2 m + 3 m). This will allow more distance for the tracking of high-momentum hadrons produced at small angles, and a larger bore angle for efficient detection of the scattered beam leptons.

The characteristics of the solenoid are guided by the desire to optimize the tracking resolution, which at central angles scales like $\Delta p/p \sim \sigma p/BR^2$, where σ is the position resolution, p the particle momentum, B the magnetic field, and R the radius of the central tracker. At forward angles, however, the resolution depends on the scattering angle, but is independent of R as the particle leaves the cylindrical central tracking system from the front side (see the left panel of Fig. 29). The resolution will then deteriorate rapidly given the lack of transverse field along the central axis of a solenoid. This will later be remedied by addition of a small dipole field, as high ion energies boost the outgoing hadrons to high momenta at forward angles and one wishes to optimize resolutions also in the forward-ion direction. To obtain a roughly better than 1% momentum region for central angles and particles in the 5-10 GeV/c momentum range, a field B in the 2-4 T range seems highly desirable. This high field requirement suggests a magnet with a reasonably small diameter, preferably not larger than about 4 m, putting radial space at a premium. Of course, a

smaller diameter has the advantage of simplifying the magnet design, with the additional advantage of reducing detector cost (which scale with the radius for the barrel calorimeter and roughly as the radius squared for the endcaps). An alternate solution may be to increase the space for tracking in the central solenoid while reducing the required solenoid field, as illustrated in the right panel of Fig. 29. Here, the resolution improvement for pions with 10 GeV/c momentum and a scattering angle of 90° is shown as a function of the tracking length and solenoidal field. Thus, there is strong incentive to reduce the space requirements for Particle Identification detectors within the central solenoid as much as possible, to use available space for tracking, or reduce the solenoid diameter.

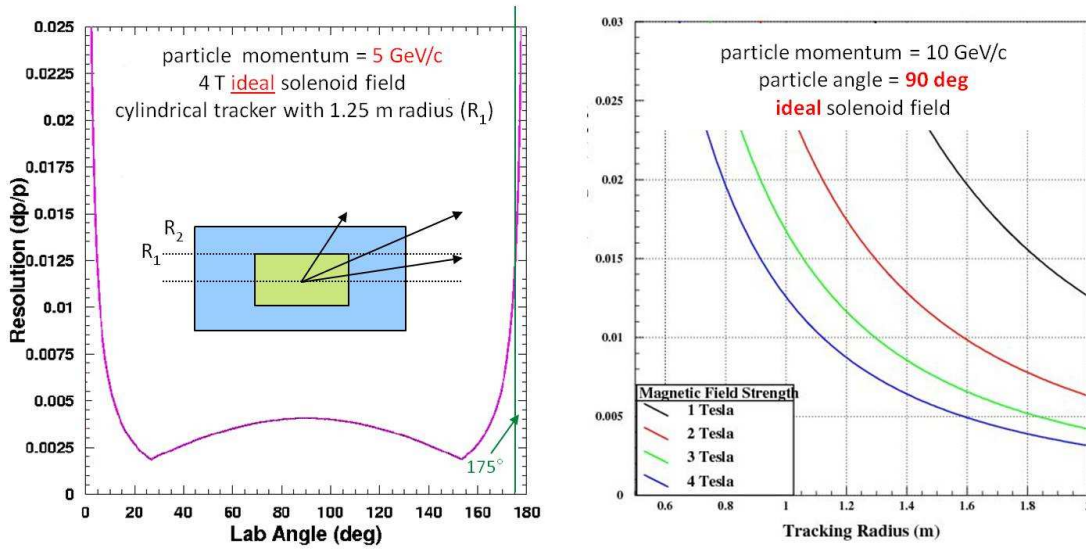


Figure 29: (left) The resolution as a function of lab angle for a particle (pion) momentum of 5 GeV/c in a 4 T ideal solenoidal field and with a cylindrical tracker of radius 1.25 m; (right) The resolution as function of solenoidal field strength and tracker radius for a particle (pion) momentum of 10 GeV/c and a scattering angle of 90° .

The central detector would contain a tracker, particle identification, and calorimetry. A three layer configuration of the central tracker was suggested at the JLab EIC detector workshop (June 4-5, 2010)¹. The first layer would consist of a low-mass vertex tracker with sufficient resolution to separate primary and secondary vertices in charm production. The middle layer would be a Time-Projection Chamber (TPC) with GEM-based readout, and the outer layer would be a cylindrical GEM tracker. The position resolution of the TPC would be about $50 \mu\text{m}$, which is a factor two improvement over the inner drift chambers of CLAS12. In conjunction with the outer GEM layer, it should provide adequate (r, θ, ϕ) information. Ongoing R&D for vertex and micropattern detectors (including GEMs), suggest that such a high-performance tracker could be built for the EIC detector. Nevertheless, a radius of at least 1 m would be required.

Particle identification in the central detector is the most open design question. At low momenta, dE/dx (in the TPC) or TOF can be helpful. With precise timing, the momentum range of the latter could be extended somewhat (although this would require a

¹<http://conferences.jlab.org/eic2010>

comparable uncertainty on the track length determination in order to get a good t_0). The most challenging requirement is, however, for a radially compact detector providing π/K identification over a sufficiently wide momentum range. Taking up 8 cm of radial space, a BaBar-type DIRC could satisfy this condition, providing 3σ π/K separation up to 4 GeV/c, e/π separation close to 1 GeV/c, and p/K separation up to 7 GeV/c. An aerogel barrel RICH could provide almost comparable performance. Neither is sufficient for the exclusive (GPD) or semi-inclusive (TMD) programs. The current baseline design thus includes a Low-Threshold Cerenkov Counter (LTCC) with C_4F_{10} or C_4F_8O gas in addition to the DIRC. This would provide e/π separation between 1 and 3 GeV/c, and π/K separation from 4 to 9 GeV/c, but at a price of 50-70 cm of radial space. Adding C_4F_{10} to a barrel RICH would increase the radius by at least 80-90 cm, although a RICH could extend the momentum coverage to 14 GeV/c. Ultimately the allocation of radial space to PID and tracking is a matter of priorities, and with multiple detectors one could easily imagine that these would offer complementary capabilities. On the other hand, if one could improve the θ_c resolution for a DIRC by about a factor of two, its 3σ π/K separation could be extended to about 6 GeV/c, with the upper limits for the other particle species shifting accordingly, eliminating the need for the gas Cerenkov. Given the size of the EIC detector, an all-crystal electromagnetic calorimeter would be financially expensive and only needed in critical regions. Tungsten powder / scintillating fiber or other technologies may provide a more affordable alternative for the barrel without an excessive loss of resolution. If needed, the return yoke of the solenoid magnet can be used as part of a hadronic calorimeter, and as an absorber for muon detection (along the lines of CMS).

1.4.5 Detector Endcaps

The electron side endcap would face requirements quite similar to those of CLAS12, and it is natural to adopt a similar design. Due to the offset of the IP, lower particle momenta, and simpler small-angle detection (see section 1.4.6), the electron side is not nearly as crowded as the ion one. For lepton detection at small polar angles (θ), the main priority of the tracking would be to provide good θ resolution, as this directly impacts the reconstruction of the event kinematics. The inner part of the endcap tracker should thus be an extension of the vertex tracker, using semiconductor detectors. At larger angles, the requirements are not as demanding and the choice of technology is not as crucial. It could include planar GEMs or even cheaper drift chambers with a small cell size. Given the generous space constraints, a final tracking region could be added outside of the solenoid itself to improve tracking performance. Lepton identification will also use an electromagnetic calorimeter and a High-Threshold Cerenkov Counter (HTCC) with CF_4 gas or equivalent. The light can be collected by mirrors, producing a cost-effective readout. In this endcap region, hadron identification will be partially provided by a TOF detector, for which the endcap is more suitable than the barrel due to the longer flight path. The π/K identification range, again in the electron endcap region, could be extended through the use of a Low-Threshold Cerenkov Counter (LTCC) with C_4F_8O gas or equivalent, possibly operating slightly above atmospheric pressure to lower the pion detection threshold. Of course, to push π/K identification to larger momenta, ~ 10 GeV/c, a RICH detector may need to be considered, but there does not seem to be a compelling need in this electron endcap region for the MEIC. Given the space available on the electron side, there is no strong requirement for a compact electromagnetic calorimeter. Since the momentum resolution from tracking deteriorates at small angles, where also the rates go up, the ideal configuration would involve

an inner circle of high-resolution, radiation-hard crystals, and a more budget-friendly outer part. Both could be covered by the same pre-shower calorimeter.

The ion side endcap would have to deal with hadrons with a wide range of momenta, some approaching that of the ion beam. The forward tracking would thus greatly benefit from good position resolution (e.g., planar GEMs), at least on par with the $50\ \mu\text{m}$ of the TPC. The smallest angles can be covered by semiconductor detectors as on the electron side. Of course, a good position resolution will also put significant demands on the detector alignment and field knowledge. The most important feature of the forward tracker, however, is related to the ion beam crossing angle with respect to the electron beam. In addition to being a key component of the small-angle detection, this turns the tracking resolution into a 2D problem. Whereas the momentum resolution in a solenoidal field deteriorates rapidly as small angles with respect to the axis, the hadron scattering angle is essentially defined with respect to the ion beam line. Given that the proton/ion beam traverses the solenoid at a $50\ \text{mr}$ (crab crossing) angle, so already encounter some transverse magnetic field component, hadrons scattered away from the electron beam will end up in a part of the detector with better momentum resolution than those scattered towards the electron beam. Taking the 2D character of the problem into account, and the significant $50\ \text{mr}$ beam crossing angle, the spot of poor resolution will be moved into the periphery covering and only a small range in the azimuthal angle ϕ will be affected. For most processes, all particle tracks will remain in the zone of good resolution. In contrast, if the crossing angle is small, all particle tracks at very forward angles will suffer from poor momentum resolution, as shown in the right panel of Fig. 29.

To identify particles of various species over the full momentum range, one would ideally want to use several radiators. A typical combination could include aerogel (perhaps with more than one index of refraction), C_4F_{10} or equivalent gas, and CF_4 . This would make some kind of RICH detector an attractive option, in particular if the endcap radius was not too large. Still, there are several possible approaches which eventually will need to be studied in detail. One could, for instance, imagine a dual radiator gas RICH combined with a disk DIRC (as in PANDA), with the latter providing π/K identification up to about $4\ \text{GeV}/c$. Having the longest flight path from the IP, the ion endcap is also where one could achieve the best results with high-resolution TOF (perhaps even integrated with the readout of the RICH). Regardless of technical solution, the total thickness of the stack of PID detectors is assumed not to exceed $1.5\ \text{m}$. Calorimetry in the ion endcap will include both electromagnetic and hadronic parts. The main focus of the former will be to study various reaction products rather than the scattered lepton. However, the same resolution arguments apply as for the electron endcap, and a solution with an inner high-resolution circle, and a more cost-effective outer part makes sense here as well. The magnetic enclosure of the endcap can, as in the case of the return yoke of the central detector, be integrated with a hadronic calorimeter, and serve as an absorber for muon detection.

1.4.6 Small-angle Detection

The design for the full-acceptance detector envisions small-angle detection on both sides of the central detector. The naming convention used here will be that the “ion side” or “ion endcap” refers to the side of the outgoing ion and incoming electron beam. The “electron side” refers to the other one.

On the ion side, the detection will be performed in three stages as illustrated in Figure 30. The first stage is the endcap (discussed in section 1.4.5), which will cover all angles down

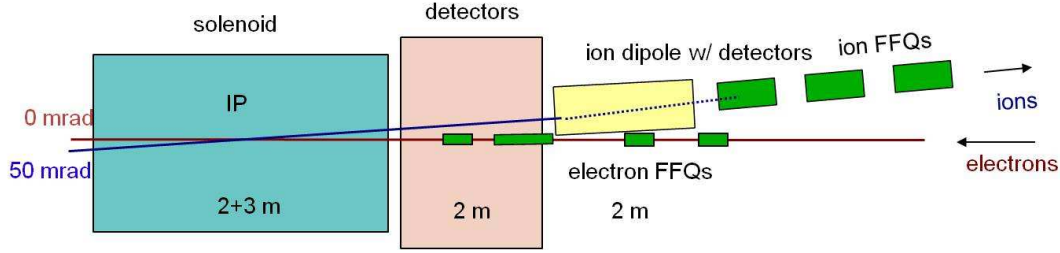


Figure 30: Forward ion detection with 50 mrad crossing angle for the full-acceptance detector. Note that the distance to the final focusing quadrupoles are located 7 m from the IP.

to the acceptance of the forward spectrometer. This in turn has two stages, one upstream of the ion Final Focus Quadrupoles (FFQs), covering down to 0.5° , and one downstream covering up to at least 0.5° . The former will use a 1-2 Tm dipole to augment the solenoid in the range where the resolution is poor. The magnet will be about 1 m long and cover the distance to the electron beam (corresponding to the horizontal crossing angle of 50 mrad), and about twice that in the other directions, for a total acceptance of 150 mrad in the horizontal and 200 mrad in the vertical plane. An important feature of the magnet design is to ensure that the electron beam line stays field free. The dipole will have trackers at the entrance and exit, and a calorimeter covering the ring-shaped area in front of the first ion FFQ. For neutrons, the primary goal of this calorimeter is to have good angular resolution. This intermediate stage is essential for providing good coverage and resolution in $-t$, and to investigate target fragmentation. The former is of particular importance for the study of exclusive processes, essential for the 3D imaging of the nucleon, requiring detection of the recoil baryon. Since $t \sim \theta_p^2 E_p^2$, the t -resolution depends on the angular resolution that can be achieved. With a 50 GeV proton beam, a $-t$ of 1 GeV^2 corresponds to about 27 mrad (see Fig. 27). With an angular resolution of 1 mrad, the intermediate detection stage would be able to cover $-t$ up to 2 GeV^2 with a resolution of about $40\text{-}50 \text{ MeV}^2$ a value that would scale with angular resolution of the inner silicon forward tracker. Recoil baryons with larger values of $-t$ would be detected in the endcap. At higher ion beam energies the t -acceptance of the dipole increases, but the resolution deteriorates rapidly (due to the E_p^2 factor). Going to lower ion energies, the opposite is true.

The last stage is the ultra-forward detection that is crucial for the tagging of spectator protons in deuterium, as well as other recoil baryons/nuclei. The design is heavily integrated with the accelerator (see figure 31), using two key features. One is, again, the horizontal crossing angle for the ion beam, which needs to be “corrected” some distance downstream of the interaction point (IP). For a 50 mrad crossing angle, this corresponds to a bend of close to 100 mrad, and the required 20 Tm dipole(s) can also serve as a dedicated forward spectrometer, using the long drift space beyond for detection of both charged and neutral particles. The other feature is a beam optics requiring low quadrupole gradients, allowing large aperture magnets. In the current design, the maximum quad gradient is less than 65 T/m. With a 10 cm aperture, this creates a 6.5 T peak field (simply the product of the aperture radius and gradient), which the magnet design should be able to support if larger peak fields were acceptable, the apertures would increase accordingly. The gradients are further arranged so that they drop off faster than the distance from the IP to that specific

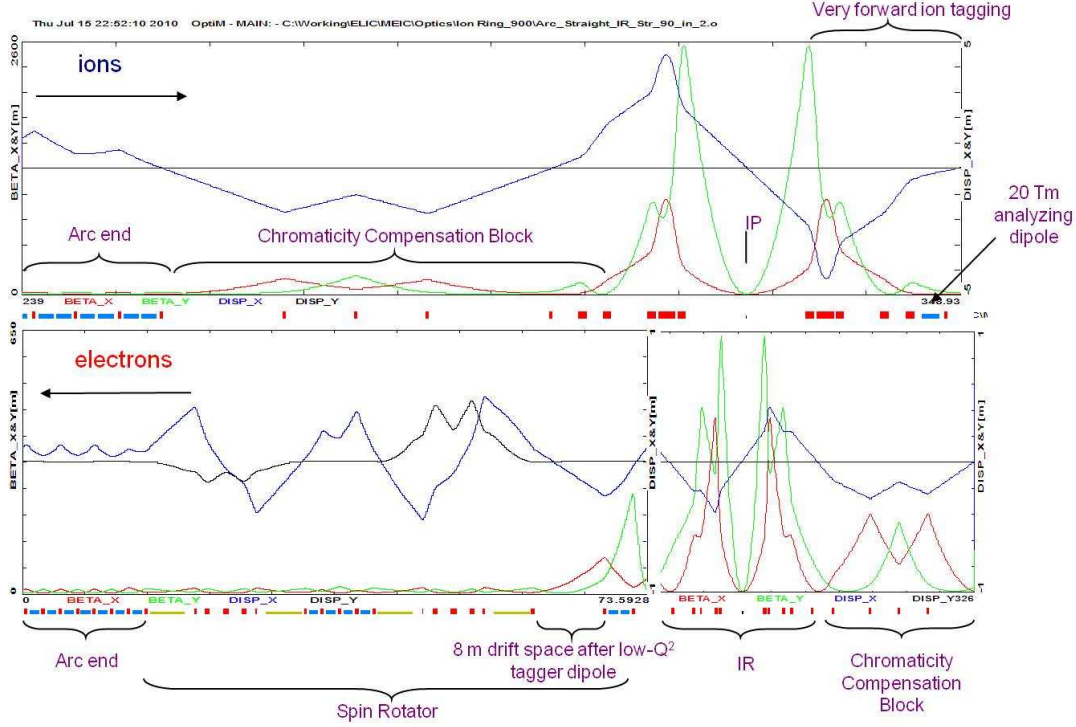


Figure 31: The integration of particle detection in the accelerator.

location, allowing the apertures to become correspondingly larger, and thereby making sure that no bottlenecks are created. This defines a geometrical acceptance through the ion final-focusing quads (FFQs) of 10 mrad, or well beyond 0.5° , on each side of the beam (20 mrad in total). To focus the 250 GeV beams in ELIC, the maximum quadrupole gradients would have to be 2.5 times larger than for the 100 GeV of the MEIC, and the apertures reduced accordingly.

The acceptance for charged particles depends on both the polar and azimuthal angles (since quads focus in one plane and defocus in the other), as well as their momentum. This can be optimized by placing a dipole spectrometer relatively close to the FFQs. To give a numerical example, a 100 mrad bend to a deuterium beam would equate to a 200 mrad bend for a spectator proton. Over a drift space of 10 m (a relatively modest distance), the spectator proton would acquire a transverse separation of 1 m from the main beam. For heavy nuclei ($A/Z = 2.5$) with a negligible scattering angle at close to the beam momentum, this would increase to 1.5 m, while fragments with other A/Z ratios would be lined up in between (in particular, $N=Z$ would be at 25 cm, while neutron rich fragments would be deflected to the other side). Ions scattered at zero degrees and having 98% of the beam momentum would be 2 cm from the beam after 10 m of drift. Due to the large deflection in a well known field (including the few preceding elements), the momentum resolution of the spectrometer would be excellent. Since no position measurements would be possible within the beam-stay-clear area, the angular resolution would depend on the knowledge of the optics between the IP and detection point. The reconstruction of the angle would be aided by the scattered particles quickly exiting the beam-stay-clear area after having passed the spectrometer, with multi-point tracking to be applied in the drift region. Nevertheless,

some low-momentum particles scattered at large angles will not make it all the way to the dipole spectrometer. To detect these particles, some *ad hoc* detectors (“Roman pots”) may be placed along the way, although an interesting idea currently under investigation is to have a small-diameter compensating solenoid between the FFQs and the 20 Tm dipole. In addition to its benefits for the accelerator, such a magnet could help in tracking charged particles that do not reach the final spectrometer dipole.

The low- Q^2 tagger on the electron side will complement the electron detection in the central detector and electron side endcap. Since the electron quad gradients required for 11 GeV beams are very small compared with what is needed for 100 GeV protons, one can make the apertures very large without being constrained by peak fields (the different apertures on the incoming and outgoing sides do not affect the optics). The optimal transition point from the calorimeter to tagger coverage will ultimately be determined by physics simulations. The quads would be followed by a dipole spectrometer with sufficient drift space (8 m in the current layout) to detect leptons with a significant fraction of the beam energy.

1.4.7 Beam Helicity Reversals

The electron and ion beam polarimetry has been given a special “interaction region” in the MEIC/ELIC design, in part due to the often large amount of space needed for Compton polarimetry. With the anticipated work in systematic understanding of Compton polarimetry in both JLab Halls A and C, and further plans to cross-calibrate this with atomic beam Moller polarimetry for a future demanding parity-violating Moller experiment, electron beam polarization determination through Compton polarimetry may well achieve sub-0.5% uncertainties. Ion beam polarimetry remains more complicated, although efforts to reduce uncertainties are underway and possibilities are studied in elastic and inelastic electron-proton scattering experiments in situ.

The MEIC design will need both fast electron spin helicity reversal or flip for double-spin experiments and a program of deep-inelastic parity-violating experiments, and fast ion-spin flip for single-nucleon spin asymmetry experiments. The latter can also be an alternate method for double-spin experiments. The MEIC design, with its 750 MHz bunch trains, does not assume bunch-to-bunch spin flips, but also does not need it. A helicity-reversal frequency of 0.1 Hz will be at about the level needed for experiments.

For double-spin experiments, it is to first order equivalent to perform fast helicity reversals of electron or ions. The choice is a question of detailed precision, as shown later. For single-spin asymmetry experiments, these techniques are however totally different, and can not replace each other. Single-electron spin asymmetry (flipping electrons only) is mostly useful for parity violation experiments, while single-nucleon spin asymmetry (flipping ions) is mostly useful for nucleon transverse-spin and other TMD experiments. Both type of experiments are routinely performed at JLab, and both will become an important part of the EIC science program.

The rate of the required helicity flips is closely related to the systematic understanding of the precision. Typically, although already very difficult, one can control the systematic uncertainties between two helicity states to about 1%. To further reduce this asymmetry, to a level of 10^{-8} for the case of typical parity-violating experiments at JLab, or to a level of 10^{-5} for transverse-spin experiments, one has to provide a suppression fraction of 10^{-6} (for electron spin flip) or 10^{-3} (for ion spin flip) by fast spin flip techniques. The suppression factor by such fast helicity reversal is proportional to $1/\sqrt{N}$, where N is the number of pairs of spin flip. If we assume a typical single-nucleon spin asymmetry experiment of 3 months of

continuous running (assuming one can keep control of the systematic uncertainties between the two helicity states at the 1% level for the full period), one needs to accumulate 10^6 pairs to reach a suppression of 1000, or about 8 flips per minute. This is the root of the present 0.1 Hz beam helicity reversal assumption mentioned above.

List of Authors

E.C. Aschenauer

Physics Department, Brookhaven National Laboratory, Upton, NY 11973, USA

R. Ent

Jefferson Laboratory, Newport News, VA 23606, USA

T. Horn

Catholic University of America, Washington, DC 20064, USA

P. Nadel-Turonski

Jefferson Laboratory, Newport News, VA 23606, USA

H. Spiesberger

Institute for Physics, Johannes-Gutenberg-University, D-55099 Mainz, Germany

References

- [1] A. B. F. Jacquet, Proceedings of the Study of an ep facility for Europe, Ed. U. Amaldi, 391, DESY 79/48.
- [2] U. Bassler and G. Bernardi, Nucl. Instrum. Meth. **A361**, 197 (1995), hep-ex/9412004.
- [3] (Spin Muon Collaboration), B. Adeva and other, Phys. Rev. D **62**, 079902 (2000).
- [4] A. Caldwell and H. Kowalski, Phys. Rev. C **81**, 025203 (2010).
- [5] H. Spiesberger *et al.*, Contribution to Workshop on Physics at HERA, Hamburg, Germany, Oct 29-30, 1991.
- [6] I. Akushevich and H. Spiesberger, Contribution to Workshop on Future Physics at HERA (1991).
- [7] M. Hirai, S. Kumano, and T. H. Nagai, Phys. Rev. **C76**, 065207 (2007), 0709.3038.
- [8] K. J. Eskola, V. J. Kolhinen, and C. A. Salgado, Eur. Phys. J. **C9**, 61 (1999), hep-ph/9807297.
- [9] K. J. Eskola, H. Paukkunen, and C. A. Salgado, JHEP **07**, 102 (2008), 0802.0139.
- [10] K. J. Eskola, H. Paukkunen, and C. A. Salgado, JHEP **04**, 065 (2009), 0902.4154.
- [11] H. Spiesberger, Phys. Rev. **D52**, 4936 (1995), hep-ph/9412286.

- [12] J. Kripfganz, H. Mohring, and H. Spiesberger, Z. Phys. **C49**, 501 (1991).
- [13] G. Gaycken *et al.*, Nucl. Instrum. Meth. **A560**, 44 (2006).
- [14] C. Hu-Guo *et al.*, JINST **4**, P04012 (2009).
- [15] J. de Favereau, X. Rouby, and K. Piotrkowski, JINST **2**, P09005 (2007), 0707.1198.
- [16] E. Perez, L. Schoeffel, and L. Favart, (2004), hep-ph/0411389.
- [17] R. J. Charity, Phys. Rev. **C82**, 014610 (2010), 1006.5018.
- [18] A. Botvina, G. Chaudhuri, S. Das Gupta, and I. Mishustin, Phys. Lett. **B668**, 414 (2008), 0805.3514.
- [19] M. Beckmann *et al.*, Nucl. Instrum. Meth. **A479**, 334 (2002), physics/0009047.
- [20] A. Zelenski *et al.*, in Proceedings of the 18th International Symposium on High-Energy Spin Physics, Charlottesville, 2008, AIP Conf. Proc. No 1149 , p. 847. .
- [21] A. Zelenski *et al.*, Nuclear Instruments and Methods in Physics Research Section A: Accelerators, Spectrometers, Detectors and Associated Equipment **536**, 248 (2005), Polarized Sources and Targets for the 21st Century. Proceedings of the 10th International Workshop on Polarized Sources and Targets.
- [22] Y. Makdisi *et al.*, Proc. of PAC07, p. 4671 .
- [23] *PHENIX Collaboration, The PHENIX Experiment at RHIC - Decadal Plan 2011 - 2020.*
- [24] K. H. Ackermann *et al.*, Nuclear Instruments and Methods in Physics Research Section A: Accelerators, Spectrometers, Detectors and Associated Equipment **499**, 624 (2003), The Relativistic Heavy Ion Collider Project: RHIC and its Detectors.
- [25] M. Anderson *et al.*, Nuclear Instruments and Methods in Physics Research Section A: Accelerators, Spectrometers, Detectors and Associated Equipment **499**, 659 (2003), The Relativistic Heavy Ion Collider Project: RHIC and its Detectors.
- [26] M. Anderson *et al.*, Nuclear Instruments and Methods in Physics Research Section A: Accelerators, Spectrometers, Detectors and Associated Equipment **499**, 679 (2003), The Relativistic Heavy Ion Collider Project: RHIC and its Detectors.
- [27] Star collaboration, decadal plan.